

File ID 445725
Filename Thesis

SOURCE (OR PART OF THE FOLLOWING SOURCE):

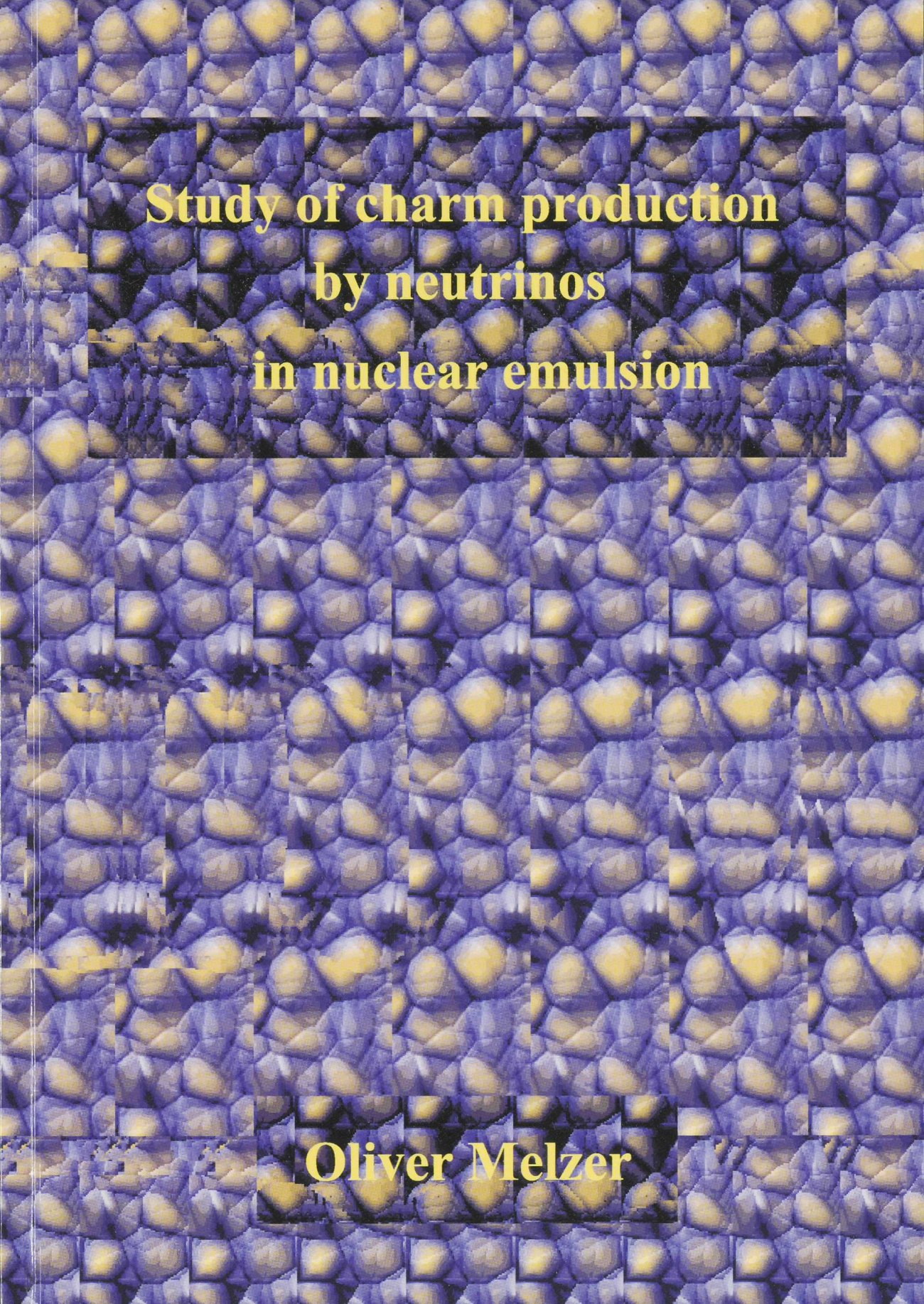
Type Dissertation
Title Study of charm production by neutrinos in nuclear emulsion
Author O. Melzer
Faculty Faculty of Science
Year 2001
Pages 98

FULL BIBLIOGRAPHIC DETAILS:

<http://dare.uva.nl/record/96013>

Copyright

It is not permitted to download or to forward/distribute the text or part of it without the consent of the author(s) and/or copyright holder(s), other than for strictly personal, individual use.



**Study of charm production
by neutrinos
in nuclear emulsion**

Oliver Melzer

**Study of charm production
by neutrinos
in nuclear emulsion**

ACADEMISCH PROEFSCHRIFT

ter verkrijging van de graad van doctor
aan de Universiteit van Amsterdam
op gezag van de Rector Magnificus
Prof. Dr. J.J.M. Franse
ten overstaan van een door het
college voor promoties ingestelde commissie,
in het openbaar te verdedigen
in de Aula der Universiteit
op woensdag 11 april 2001, te 10.00 uur

door

Oliver Melzer

geboren te Rendsburg, Duitsland

promotor: Prof. Dr. J.J. Engelen

co-promotor: Dr. R. van Dantzig

Faculteit der Natuurwetenschappen, Wiskunde en Informatica

The work described in this thesis is part of the research program of 'het Nationaal Instituut voor Kernfysica en Hoge-Energie Fysica (NIKHEF)' in Amsterdam, the Netherlands. The author was financially supported by 'de Stichting voor Fundamenteel Onderzoek der Materie (FOM)', which is funded by 'de Nederlandse Organisatie voor Wetenschappelijk Onderzoek (NWO)'.

The front cover illustration can be viewed as a piece of art, a beautiful picture generated by a computer. However, information invisible in two dimensions has been hidden inside the image. Very similar to nuclear emulsion scanning, in two dimensions only limited information can be extracted. To obtain the full information, a third dimension is needed. To see the hidden three-dimensional stereogram image one should relax the eyes and allow the point of focus to move behind the surface of the cover. It might be helpful to put the face close to the image, staring right through the booklet, and slowly move away from the cover, still staring ahead. If the focus is at the correct point, the three-dimensional image will become visible and the hidden information can be decrypted.

Contents

1	Introduction	1
2	Charm production in neutrino charged current interactions	7
2.1	Kinematics	8
2.2	Deep inelastic charm production	10
2.3	Diffractive charm production	14
2.4	Leptonic decays of charmed hadrons	15
2.5	Present experimental status	18
3	The CHORUS experiment	23
3.1	Neutrino beam	24
3.2	The experimental setup	26
3.2.1	Target area	26
3.2.2	Hadron spectrometer	28
3.2.3	Honeycomb chamber	29
3.2.4	Calorimeter	29
3.2.5	Muon spectrometer	31
3.2.6	Trigger system	32
3.3	Emulsion target	33
3.3.1	Track formation	34
3.3.2	Emulsion shrinkage and track distortion	34
3.3.3	Swelling of emulsion	35
3.3.4	Automatic scanning	36
3.3.5	Scanning procedure	37
3.3.6	Manual scanning	39
3.4	Event reconstruction	40

4	Deep inelastic charm production	43
4.1	Analysis procedure	43
4.1.1	Classification of neutrino events	43
4.1.2	Correcting the data	45
4.1.3	Event generation and detector response	49
4.1.4	Charm event selection	52
4.2	Results	54
4.2.1	Charm topologies	54
4.2.2	Charm kinematics	58
4.2.3	Charm cross section	58
4.2.4	Neutral charm versus charged charm	65
4.2.5	Charm quark mass	67
4.2.6	Charm fragmentation	68
4.2.7	Strange sea	70
4.2.8	Weak mixing V_{cd}	74
5	Diffractive charm production	77
5.1	Selection of diffractive D_s^* events	77
5.2	Background study	78
5.3	Detector acceptance and reconstruction efficiency	78
5.4	Reconstruction of a candidate event	79
5.5	Limit on the ν_τ mass	83
5.6	Cross section	84
	Summary	87
	Samenvatting	89
	Acknowledgements	97

Chapter 1

Charming neutrinos

I have committed the ultimate sin, I have predicted the existence of a particle that can never be observed.

Wolfgang Pauli [1]

Neutrinos are not only charming but also very peculiar particles: postulated by a theorist, detected in an experiment and studied now for 40 years. But still today neutrinos remain enigmatic, newspapers title it *The Ghost Particle* and they are subject of research for many experiments all around the world.

In the work described in this thesis some properties of neutrinos have been studied, in particular concerning their interaction with matter. It emphasizes that neutrinos are not only charming themselves but that they can also produce so called *charmed particles*.

In the following introduction we give an overview of the intriguing field of neutrino physics.

How did it all start?

In the beginning of the 20th century a fundamental problem teased the physicist: in certain radioactive decays the energy did not seem to be conserved. In 1931 Wolfgang Pauli suggested that this missing energy could be carried away by an unknown neutral particle which was escaping detection. In 1934 Enrico Fermi developed a comprehensive theory of radioactive decays, including Pauli's hypothetical particle and coined it *neutrino* (which means in Italian *little neutron*). Since the neutrino (ν) interacts very weakly with matter it took until 1959 to observe it. In that year Clyde Cowan and Fred Reines detected the neutrino for the first time in an experiment. For this discovery they received

Family	Flavour		Electric Charge	Mass (MeV) ¹
First	(anti-)electron	$e^- (e^+)$	-1 (+1)	0.511
	electron (anti-)neutrino	$\nu_e (\bar{\nu}_e)$	0	$< 3 \times 10^{-6}$
Second	(anti-)muon	$\mu^- (\mu^+)$	-1 (+1)	105
	muon (anti-)neutrino	$\nu_\mu (\bar{\nu}_\mu)$	0	< 0.19
Third	(anti-)tau	$\tau^- (\tau^+)$	-1 (+1)	1777
	tau (anti-)neutrino	$\nu_\tau (\bar{\nu}_\tau)$	0	< 18.2

Table 1.1: The lepton families.

the 1995 Nobel Prize in physics. Since the discovery, in numerous experiments it was tried to measure properties of the neutrino and to find answers to various questions. Is the neutrino stable? Are there other neutrino species? Is the neutrino its own antiparticle? Does a neutrino have a mass? How and where are neutrinos produced? Does the neutrino have a magnetic moment? How do neutrinos interact with matter? It goes beyond the scope of this thesis to give the status of the answers to all of these questions, but a comprehensive overview can be found in Reference [2]. One of the questions that is discussed in detail in this thesis is how neutrinos interact with matter and how they can produce charmed particles.

How does the neutrino fit into today's picture of the world?

In 1962 experiments at Brookhaven and CERN made a surprising discovery: there are at least two types of neutrinos. One is associated with the electron (e), the other with the muon (μ), the heavier partner of the electron. Later in 1975 a third type (flavour) of particle from this *lepton* family was found, the tau (τ) particle. The existence of the corresponding tau neutrino was already fully accepted for many years because of indirect evidence [3], before it was directly observed in 2000 by an experiment at Fermilab [4]. All leptons have anti-particles; this completes our present picture of three lepton families as represented in Table 1.1.

Not only in the neutrino field but also in other sectors of particle physics dramatic progress has been made during the past decades. In an experiment in 1968 at the Stanford Linear Accelerator (SLAC) it was found that nucleons, when probed at high space-time resolution, contain partons, later identified as quarks. Hence, the leading theoretical description is called the Quark-Parton-Model (QPM). Particles called *baryons*, such as the proton, are bound states of

¹Throughout this thesis the natural system of units is used where $\hbar = c = 1$

Family	Flavour		Electric Charge	Mass (MeV)
First	(anti-)up	u (\bar{u})	+2/3 (-2/3)	4
	(anti-)down	d (\bar{d})	-1/3 (+1/3)	7
Second	(anti-)charm	c (\bar{c})	+2/3 (-2/3)	1.3×10^3
	(anti-)strange	s (\bar{s})	-1/3 (+1/3)	170
Third	(anti-)top	t (\bar{t})	+2/3 (-2/3)	1.7×10^5
	(anti-)bottom	b (\bar{b})	-1/3 (+1/3)	4.4×10^3

Table 1.2: The quark families.

three quarks; *mesons* are composed of a quark and an antiquark.

The quarks and anti-quarks also come in three families and their (trivial) names can be found in Table 1.2. In the QPM, the nucleon contains three *valence* quarks surrounded by a *sea* of virtual quark-antiquark pairs. For instance, the valence quarks of the proton are two u quarks, each with electric charge 2/3, and one d quark with charge -1/3, whereas the sea can consist of all quark-antiquark flavours.

Both, quarks and leptons, are fermions with half integer spin (intrinsic angular momentum).

Furthermore, it has been found that all interactions in nature are governed by four fundamental forces: the electromagnetic, weak, strong and gravitational force. They are all four² mediated by bosons (with integer spin) summarized in Table 1.3.

Neutrinos are only subject to the weak force. In the case of a (charged) W exchange the interaction is denoted as charged current (CC), in the case of a (neutral) Z exchange as neutral current (NC).

In a CC interaction, there is a transition between different quark flavours. In technical terms, the quark mass eigenstates are no weak flavour eigenstates but linear combinations of these (flavour mixing). This results in particular

²Until today no quantum theory for gravity has been developed. Hence, the graviton is only a hypothetical particle.

Force	Mediator	Relative Strength	Range (m)
strong	gluon (g)	1	$\leq 10^{-15}$
electromagnetic	photon (γ)	10^{-2}	∞
weak	W^\pm and Z^0	10^{-5}	10^{-18}
gravity	graviton (G)	10^{-42}	∞

Table 1.3: The known forces.

probabilities for different transitions. Important for charm production, the subject of this thesis, are the CC quark flavour transitions $d \rightarrow c$ and $s \rightarrow c$. Experimentally it has been observed that transitions between quark flavours of different families are less probable than transitions within the same family. This experimental phenomenon is called Cabibbo suppression, and thus charm production on d quarks is Cabibbo suppressed with respect to the production on s quarks. The flavour mixing for all quark transitions is expressed in a 3×3 matrix, called the Cabibbo-Kobayashi-Maskawa (CKM) matrix and can be parameterized by three mixing angles and a phase [5].

When neutrinos interact with matter, another concept becomes important: the detailed theoretical description of the internal dynamics of the nucleon. This can be well described by Quantum Chromodynamics (QCD), the fundamental theory of strong interactions. In analogy with Quantum Electrodynamics (QED), the theory of the electromagnetic force, in QCD the quarks and gluons carry a 'charge' called *colour* being responsible for the strong force. Colour comes in three varieties, usually denoted as 'red', 'blue' and 'green'. Since the gluons carry colour themselves, they can interact not only with quarks but also with other gluons. Single bare quarks have not been observed in a detector. They are *confined* in colour neutral ('white') hadrons, the colour force increasing with inter-quark distance. However, for increasingly smaller distances the inter-quark coupling becomes weaker and the quarks behave as if they are almost free. This phenomenon is called *asymptotic freedom* and it allows the use of perturbation theory within QCD at small distances. *Structure functions* expressed in terms of quark and gluon distribution functions are used to describe the structure of hadrons in scattering processes on nucleons.

Are neutrinos oscillating?

No overview of the field of neutrino physics is complete without a discussion of the recent compelling evidence for neutrino oscillations, in particular coming from the Super-Kamiokande [6] experiment in Japan. Here neutrinos are measured that are generated by cosmic rays in the Earth's atmosphere. After decades of theoretical expectations and earlier experimental indications (see Reference [7] for a review), the experiment finds a specific neutrino flavour (ν_μ) *disappearing*.

The most natural explanation is that the neutrino flavour can change temporarily from ν_μ to ν_τ . The latter neutrinos are not detected in the Super-

Kamiokande experiment. Theoretically the possibility that neutrinos *oscillate* between flavours implies that at least one of them has a non-zero mass.

The CHORUS experiment was designed to search for this $\nu_\mu \rightarrow \nu_\tau$ oscillation phenomenon. It uses the CERN neutrino beam and investigates a different regime of mass and mixing parameters than the Super-Kamiokande experiment. The CHORUS experiment does not observe a signal for neutrino oscillation within its accessible parameter space, which is different from that of the Super-Kamiokande experiment. More details of the present CHORUS oscillation search result can be found in Reference [8].

What is in this thesis?

The thesis is structured as follows. After the current introductory chapter, in Chapter 2 a theoretical introduction is given on charm production by neutrinos. Furthermore, an overview of the present experimental situation can be found there. Chapter 3 describes the experimental setup of the CHORUS detector and explains the state-of-the-art scanning techniques of nuclear emulsion. Chapter 4 deals with our study of deep-inelastic charm production, whereas in Chapter 5 a different charm production process, diffractive production, is discussed.

In summary, the research reported in this thesis has been performed to increase our insight concerning properties of the neutrino in relation to the quark structure of the nucleon. Not only the knowledge itself is important and interesting, but also the consequences it has for the understanding of the world around us.

Quoting a recent paper [9], "[...] *The relic tau neutrinos [may] have sufficient energy density to close the **university***", the impact of neutrino properties may even be larger for society than usually assumed.

...the ... of the ...

The ... of the ...

What is ...

The ... of the ...

...the ... of the ...

...the ... of the ...

...the ... of the ...

...the ... of the ...

...the ... of the ...

...the ... of the ...

...the ... of the ...

...the ... of the ...

...the ... of the ...

...the ... of the ...

...the ... of the ...

...the ... of the ...

...the ... of the ...

Chapter 2

Charm production in neutrino charged current interactions

*Things should be made as simple as possible,
but not any simpler.*
Albert Einstein

Charm production by neutrinos has been investigated in several experiments in the past. Modern detector technologies have recently allowed to increase statistics significantly. Hence, mechanisms and kinematics of heavy flavour production as well as of hadronization and of weak decays can be studied in more detail. In most of the experiments, charm production is studied in the regime of deep inelastic interactions related to perturbative QCD. In deep inelastic scattering (DIS), where the four-momentum transfer Q^2 is much larger than the nucleon mass ($Q^2 \gg M^2$), neutrinos - like charged leptons - are used as a point-like probe to study the parton structure of the nucleon. On the other hand, at small Q^2 values ($Q^2 \lesssim M^2$) long range processes become important where scattering processes can take place on nucleons or nuclei as a whole. The knowledge of this non-perturbative regime where neutrino-induced diffractive charm production takes place is sparse because it is experimentally difficult to access. In our work for the first time both production processes are studied together in an emulsion experiment.

Recent results from HERA indicate that also 'hard diffraction' occurs in DIS: the nucleon does not break up even for $Q^2 \gg M^2$. The 'soft' scale is then governed by the four-momentum difference squared (t) of the initial and

final state nucleon. Observation of such events in neutrino scattering would, of course, also be very interesting.

In this chapter the kinematic variables are introduced and the main theoretical aspects of deep inelastic and diffractive charm production are described. Furthermore, because in the analysis we concentrate on leptonic charm decays, the theory of weak decays of charm particles is summarized. In the last section an overview of the present experimental situation in the field of charm production by neutrinos is given.

2.1 Kinematics

In the following the charged-current (CC) reaction $\nu_\mu N \rightarrow \mu^- X$ is described in detail, where N is a nucleon and where X describes the hadronic final state. The diagram for this process is given in Figure 2.1. The four-momenta intro-

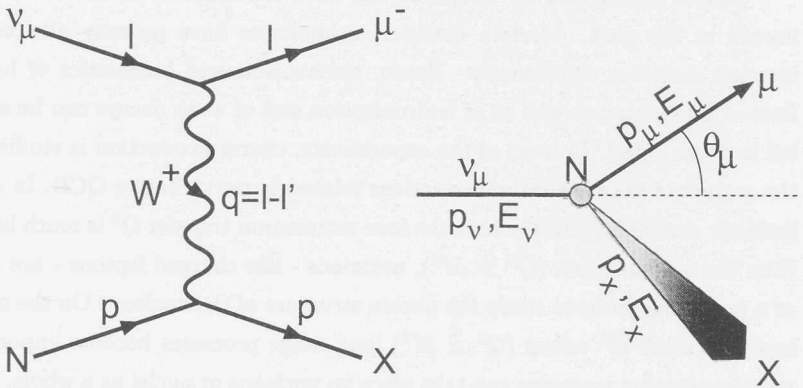


Figure 2.1: Feynman-diagram for the CC interaction $\nu_\mu N \rightarrow \mu X$ (left) and the corresponding kinematic representation in the laboratory frame (right).

duced are l for the incoming neutrino, l' for the muon, p for the nucleon and p' for the hadronic final state. With the four-momentum transfer $q = l - l'$ carried

by a W -boson (wavy line) the Lorentz invariant kinematic variables are:

$$\begin{aligned}
 Q^2 = -q^2 = -(l - l')^2 & \quad \text{Square of the four-momentum transfer} \\
 \nu = \frac{p \cdot q}{\sqrt{p \cdot p}} & \quad \text{Leptonic energy transfer} \\
 W^2 = p'^2 & \quad \text{Square of hadronic final state invariant mass} \\
 s = (l + p)^2 & \quad \text{Square of center-of-mass energy} \\
 x = \frac{Q^2}{2p \cdot q} & \quad \text{Bjorken scaling variable} \\
 y = \frac{p \cdot q}{p \cdot l} & \quad \text{Inelasticity variable}
 \end{aligned} \tag{2.1}$$

In the parton model, x can be interpreted as the fraction of the target nucleon's longitudinal momentum carried by the struck quark.

When the Fermi motion is neglected and the nucleon is considered to be at rest, the four-momenta can be written in the laboratory frame

$$p = \begin{pmatrix} M \\ 0 \\ 0 \\ 0 \end{pmatrix}, \quad l = \begin{pmatrix} E_\nu \\ 0 \\ 0 \\ -E_\nu \end{pmatrix}, \quad l' = \begin{pmatrix} E_\mu \\ -E_\mu \sin\theta \\ 0 \\ -E_\mu \cos\theta \end{pmatrix}, \tag{2.2}$$

where M is the nucleon rest mass, E_ν the neutrino energy, E_μ the muon energy and where θ corresponds to the angle between muon and neutrino momenta.

Assuming the muon mass to be small with respect to $|Q|$, the kinematic variables become in the laboratory frame

$$\begin{aligned}
 Q^2 &= 4E_\nu E_\mu \sin^2 \frac{\theta}{2} \\
 \nu &= E_\nu - E_\mu \\
 W^2 &= M^2 + 2M\nu - Q^2 \\
 s &= M^2 + 2ME_\nu \\
 x &= \frac{Q^2}{2M\nu} \\
 y &= \frac{\nu}{E_\nu}.
 \end{aligned} \tag{2.3}$$

In an experiment often the true values for the kinematic variables described above cannot be measured. For instance, neutrinos coming from leptonic decays escape detection and will distort the measurement of the total energy (that should reflect the incoming neutrino energy). Therefore, we make the distinction between *visible* quantities and *true* quantities. The true quantities can be estimated on a probabilistic basis from the visible quantities by using Monte-Carlo (MC) simulations.

2.2 Deep inelastic charm production

In the DIS regime, where $Q^2 \gg M^2$, a neutrino CC interaction can produce a charm quark. However, charm quarks themselves are not detected in experiments. The charm quark has to *dress up* with other (anti-)quarks to form a 'white' hadron that is measured in the detector. In the following the concepts for DIS production of charm quarks and hadronization into charmed particles are introduced.

Neutrino-nucleon deep inelastic scattering

Assuming (like in Figure 2.1) a single W exchange in a CC interaction, the differential cross section can be written as

$$\frac{d^2\sigma^{\nu N}}{dx dy} = \frac{G_F^2 M E_\nu}{\pi} \left(\frac{M_W^2}{M_W^2 + Q^2} \right)^2 \left[2x \frac{y^2}{2} F_1(x, Q^2) + 2x F_2(x, Q^2) \left(1 - y - \frac{Mxy}{2E_\nu} \right) + x F_3(x, Q^2) y \left(1 - \frac{y}{2} \right) \right], \quad (2.4)$$

where G_F is the Fermi constant, M_W the W mass, E_ν the energy of the incoming neutrino, and where $F_{1,2,3}(x, Q^2)$ are the neutrino-nucleon structure functions [10].

In the naive QPM the neutrinos scatter off point-like spin 1/2 quarks and the structure functions are independent of the Q^2 scale. Within the framework of QCD however, the structure functions develop a Q^2 dependence to accommodate the complexity of quark-gluon and gluon-gluon interactions inside the nucleon.

Often, the cross section is written in terms of $F_2(x, Q^2)$ and $R(x, Q^2)$ (replacing $F_1(x, Q^2)$), where

$$R(x, Q^2) = \frac{F_2(x, Q^2) \left(1 + \frac{4M^2 x^2}{Q^2} \right) - 2x F_1(x, Q^2)}{2x F_1(x, Q^2)}. \quad (2.5)$$

Here R represents the ratio of the longitudinal and transverse cross sections, σ_L/σ_T of the exchanged W . The Callan-Gross relation $2x F_1 = F_2$ implying that $R(x, Q^2) = 0$ holds for $Q^2 \rightarrow \infty$, the Bjorken scaling limit.

In the QPM the structure functions are expressed in terms of momentum weighted parton distribution functions (PDFs). In the CC neutrino-nucleon structure functions at the energies of the CHORUS experiment only d -valence and d, s, \bar{u}, \bar{c} sea quarks play a role. For different quark (q_1) and anti-quark (\bar{q}_2) flavours in the scaling limit then

$$\begin{aligned}
2xF_1(x, Q^2) &\simeq F_2(x, Q^2) = xq_1(x, Q^2) + x\bar{q}_2(x, Q^2) \\
&\simeq (xd(x, Q^2) + x\bar{u}(x, Q^2) + xs(x, Q^2) + x\bar{c}(x, Q^2)) \\
xF_3 &= xq_1(x, Q^2) - x\bar{q}_2(x, Q^2) \\
&\simeq (xd(x, Q^2) - x\bar{u}(x, Q^2) + xs - x\bar{c}(x, Q^2)).
\end{aligned} \tag{2.6}$$

Assuming strong isospin symmetry and sea quark flavour independence, the PDFs of the proton (p) and neutron (n) are related: $u^n = d^p$, $d^n = u^p$, $\bar{u}^n = \bar{d}^p$ and $\bar{d}^n = \bar{u}^p$.

Charm quark production

For the specific case of charm quark production the struck quark must be a d or s quark. Taking into account the CKM-mixing, the charm structure functions take the form

$$2xF_1^c(x, Q^2) = xF_3^c(x, Q^2) = |V_{cd}|^2 xd(x, Q^2) + |V_{cs}|^2 xs(x, Q^2), \tag{2.7}$$

where V_{cd} and V_{cs} are CKM-matrix elements.

In charm production a way of accounting for heavy quark threshold effects in leading order QCD is referred to as slow rescaling [11]. The structure functions are then assumed not to scale with x but rather with

$$\xi_S = x + \frac{m_c^2}{2M\nu}, \tag{2.8}$$

where m_c is the charm quark mass.

To take further into account target mass effects, the slow rescaling model is implemented in the Nachtmann model [12] with a scaling variable

$$\xi_N = \frac{2x}{1 + \sqrt{1 + 4M^2\xi_S^2/Q^2}}. \tag{2.9}$$

In the evaluation of the structure functions accounting for target mass and charm quark mass effects together, a substitution of the Bjorken scaling variable x is made with

$$\xi = 2x \frac{1 + \frac{m_c^2}{Q^2}}{1 + \sqrt{1 + 4M^2x^2/Q^2} \left(1 + \frac{m_c^2}{Q^2}\right)}. \tag{2.10}$$

Charm quark fragmentation

Single bare quarks have not been observed. Therefore, theoretical mechanisms have been postulated to describe the process, where a quark combines with other quarks to form an observable particle. This process which we refer to as hadronization or quark *fragmentation*, is described by non-perturbative models. All fragmentation models define a fragmentation parameter $z = \frac{p_h}{p_h^{max}}$, that describes the fraction of the momentum p_h carried by a hadron with respect to the maximum momentum p_h^{max} of the hadron (i.e. the momentum of the quark) that is allowed kinematically, at the same E_ν , Q^2 and x .

The analytical form of the fragmentation function usually depends on the quark mass. For light quarks (u , d and s), the Lund parameterization [13] is mostly used, with

$$D_L(z) \propto \frac{1}{z}(1-z)^a e^{-b m_\perp/z}. \quad (2.11)$$

The parameters a and b are fitted to data from other relevant experiments and $m_\perp = \sqrt{m^2 + p_\perp^2}$ is called *transverse mass*.

For heavy quarks two alternative parameterizations are available. The Collins-Spiller [14] function

$$D_{CS}(z) \propto \left(\frac{1-z}{z} + \frac{\epsilon_{CS}(2-z)}{1-z} \right) (1+z)^2 \left(1 - \frac{1}{z} - \frac{\epsilon_{CS}}{1-z} \right)^{-2} \quad (2.12)$$

and the Peterson [15] function

$$D_P(z) \propto \frac{1}{z} \left(1 - \frac{1}{z} - \frac{\epsilon_P}{1-z} \right)^{-2}. \quad (2.13)$$

In most analyses of other experiments, the latter parameterization has been used to describe heavy quark fragmentation. For reasons of comparability we therefore use the Peterson parameterization as well.

During the fragmentation process, the emerging hadron acquires a momentum component transverse to the original direction of the charm quark with a distribution of the type

$$\frac{dN}{dp_\perp^2} \propto e^{-\beta p_\perp^2}. \quad (2.14)$$

The parameter β was measured by LEBC EHS [16] as $\beta = 1.1 \pm 0.3$ corresponding to $\langle p_T^2 \rangle = 0.9 \pm 0.2 \text{ GeV}^2$.

Experimentally, the fragmentation variable z can not be determined on an event-by-event basis for a (short-lived) charmed hadron that decays semi-leptonically into a muon and a muon neutrino, because the neutrino energy

remains undetected. However, instead of the usual fragmentation variable z , the related and measurable variable

$$z_\mu = \frac{E_{\mu^+}}{\nu} \quad (2.15)$$

is introduced, where E_{μ^+} is the energy of the muon from the charmed hadron decay. The variable z_μ plays a role similar to z in the description of the fragmentation process. The statistical relation between z_μ and z can be determined using MC simulations.

Production probabilities for charmed particle types

To describe the fragmentation of charm quarks the various fractions of the produced charmed hadron types need to be specified. They have been determined in the E531 experiment (see section 2.5). In Figure 2.2 these fractions are shown [17]. For neutrino energies above 30 GeV, values of $(60 \pm 6) \% D^0$, $(26 \pm 6) \% D^+$, $(7 \pm 5) \% D_s^+$ and $(7 \pm 4) \% \Lambda_c^+$ have been measured.

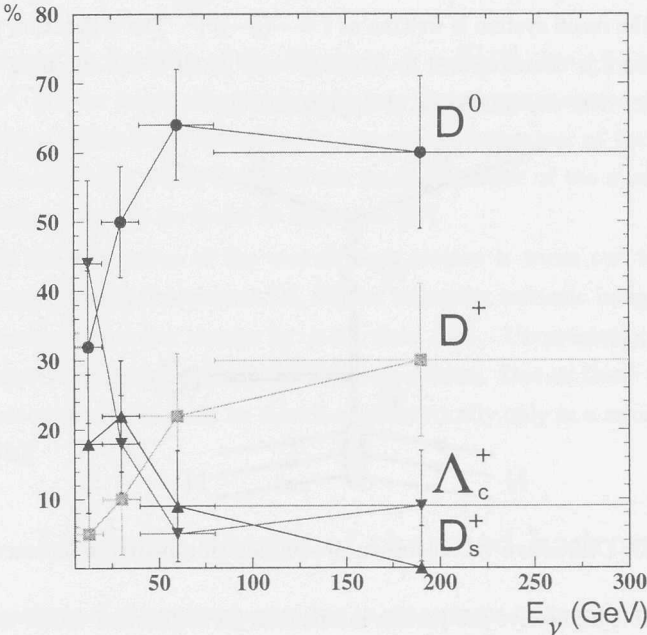


Figure 2.2: Charmed hadron production by neutrinos as measured by E531.

Towards lower energies the baryonic Λ_c fraction increases as expected from the correspondingly rising contribution of quasi-elastic processes. Folding the E531 production probabilities with the CHORUS neutrino beam spectrum results in fractions of $(55 \pm 6) \% D^0$, $(19 \pm 4) \% D^+$, $(13 \pm 9) \% D_s^+$ and $(13 \pm 7) \% \Lambda_c^+$.

2.3 Diffractive charm production

Diffraction patterns are commonly known from light wave scattering in optics. The optical diffractive pattern is characterized by a large forward (small scattering angle) peak with a series of maxima and minima for increasing scattering angles. In nuclear and high energy physics the term *diffraction* has acquired related but evolving meanings. Its main characteristics are interference, forward peaking, strong absorption, absence of internal excitation in the reaction dynamics or exchange of Pomeron-like objects (with vacuum quantum numbers).

In the context of diffractive neutrino interactions, we distinguish between diffractive *incoherent* scattering and diffractive *coherent* scattering off a nucleus. In the case of coherent diffractive scattering, the diffractive production shows an enhancement due to constructive interference of the phase coherent scattering amplitudes from the nucleons inside the target nucleus. The four-momentum transfer to the recoil system is written as $t = -(p-p')^2$. The diffraction process considered here is characterized by small Q^2 and small t , the recoiling system staying intact over the time scale of the interaction.

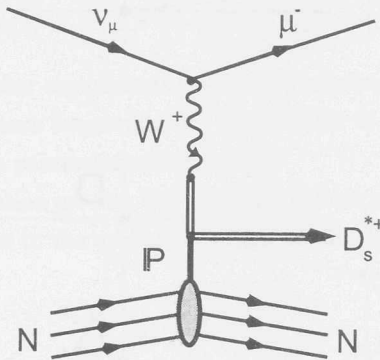


Figure 2.3: Diffractive vector meson production in a neutrino interaction.

A possible diffractive production mechanism for a charmed vector meson is shown in Figure 2.3. In a CC interaction, the virtual W -boson can transform into a $c\bar{s}$ pair that hadronically scatters off the target nucleus or nucleus as a

whole, becoming an on-shell D_s^* meson.

In our diffractive production study, in particular the Cabibbo-favoured production and leptonic decay of the vector meson D_s^* , containing a charm quark and a strange quark, is studied. The production of pseudo-scalar D_s mesons is suppressed in the kinematic domain of our experiment [18, 19, 20]. It should be mentioned that also the diffractive production of D^* mesons is possible. However, this latter process is Cabibbo-suppressed, both in the production and in the leptonic decay by V_{cd}^4/V_{cs}^4 giving in total a suppression factor of about 2.8×10^{-3} .

The cross section for diffractive vector meson production

In the framework of the (generalized) vector meson dominance (VMD) model several authors have made theoretical predictions for diffractive vector meson production [21, 22, 23, 24, 25, 26]. The generalized VMD cross section for D_s^* production can be written as

$$\frac{d\sigma}{dt} \propto \left(1 + \frac{Q^2}{m_{D_s^*}^2}\right)^{-2} Q^2 dQ^2 y(1 + \alpha) dy \left(1 + \epsilon \frac{\sigma^{L^2}}{\sigma^{T^2}}\right) e^{bt} \quad , \quad (2.16)$$

where $m_{D_s^*}$ is the mass of the D_s^* meson, $\alpha = \frac{2(1-y)}{y^2}$, $\epsilon = \frac{\alpha}{\alpha+1}$ and where σ^L and σ^T are the longitudinal and transverse virtual vector meson cross sections. The slope parameter b describes the exponential behaviour of the cross section as a function of t . More details of the implementation of the model [21] in the MC simulation can be found in Reference [27].

In the evaluation of the overall cross section it turns out that following the suggestions in References [25, 28] for adjusting intrinsic integration limits, the cross section can change by more than 30%. Uncertainties in the slope parameter enter exponentially in the cross section. Due to these uncertainties, D_s^* meson production can be described theoretically only in a semi-quantitative way [20].

2.4 Leptonic decays of charmed hadrons

The analysis of charm production has to concentrate on specific decay channels not only to get an unambiguous tag for the charmed particle but also to get an essentially background free sample. Therefore, the deep inelastic analysis focuses on the (semi-)muonic charm decays.

The diffractively produced D_s^* meson decays instantaneously [5] according to $D_s^* \rightarrow D_s \gamma$ ($B_{D_s^* \rightarrow D_s \gamma} = 0.942 \pm 0.025$) and $D_s^* \rightarrow D_s \pi^0$ ($B_{D_s^* \rightarrow D_s \pi^0} = 0.058 \pm 0.025$). The diffractive analysis is based exclusively on the subsequent leptonic decay chain $D_s \rightarrow \tau \rightarrow \mu$.

Muonic decays of charmed particles

The experimental knowledge of mass, decay length and muonic branching ratio for charmed hadrons relevant to this analysis is summarized in Table 2.1.

For the charged charmed particles the muonic branching ratios are not well known. Because in the muonic decay there is always a neutrino (but possibly also other neutrals) escaping detection, it is experimentally very difficult to simultaneously tag the particle type and measure the branching ratio. Because of this difficulty, usually a combined muonic branching ratio is determined:

$$B_{c \rightarrow \mu} \equiv B_{\sum h \rightarrow \mu} = \sum_h P_h B_{h \rightarrow \mu X}, \quad (2.17)$$

where P_h is the production probability for a specific charmed hadron $h \in (D^0, D^+, D_s^+, \Lambda_c^+)$.

Similarly, a combined muonic branching ratio for charged charmed hadrons (h^{ch}) can be defined:

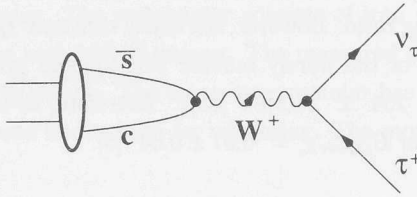
$$B_{\sum h^{ch} \rightarrow \mu} = \sum_{h^{ch}} P_{h^{ch}} B_{h^{ch} \rightarrow \mu X}, \quad (2.18)$$

where $P_{h^{ch}}$ is the production probability for a specific charged charmed hadron with respect to all charged charmed hadrons $h^{ch} \in (D^+, D_s^+, \Lambda_c^+)$.

Details about the treatment of semi-leptonic decays can be found in Reference [32]. The semi-muonic decays taken into account in the analysis are summarized in Table 2.2.

hadron	mass (MeV)	$c\tau$ (μm)	hadron $\rightarrow \mu X$ (%)
D^0	1864.5 ± 0.5	124	6.6 ± 0.8 [29]
D^+	1869.3 ± 0.5	315	17.2 ± 1.9 [30]
D_s^+	1968.6 ± 0.6	148.6	5.0 ± 5.4 [30]
Λ_c^+	2284.9 ± 0.6	61.8	4.5 ± 1.7 [31]

Table 2.1: The current knowledge of mass, decay length and muonic branching ratio of charmed hadrons.

Figure 2.4: Feynman-diagram for the decay $D_s \rightarrow \tau \nu_\tau$.

Tauonic D_s decay

Our diffractive charm production search focuses on the decay chain $D_s \rightarrow \tau \rightarrow \mu$ in order to get an unambiguous D_s tag with the double decay signature in the emulsion. Therefore, the decay $D_s \rightarrow \tau \nu_\tau$ is reviewed here.

The branching ratio for the decay $D_s \rightarrow \tau \nu_\tau$, shown in the Feynman diagram in Figure 2.4, is written as

$$B_{D_s \rightarrow \tau \nu_\tau} = \frac{G_F^2 V_{cs}^2 f_{D_s}^2 \tau_{D_s} m_\tau^2 m_{D_s}}{8\pi} \left(1 - \frac{m_\tau^2}{m_{D_s}^2}\right)^2, \quad (2.19)$$

where G_F represents the Fermi constant, V_{cs} the CKM-matrix element, f_{D_s} the decay constant, τ_{D_s} the life-time of the D_s meson, m_τ the mass of the τ lepton and m_{D_s} the mass of the D_s meson.

decay channel	branching ratio	decay channel	branching ratio
$D^0 \rightarrow \mu^+ \nu_\mu K^-$	0.032	$D^+ \rightarrow \mu^+ \nu_\mu K^0$	0.07
$D^0 \rightarrow \mu^+ \nu_\mu K^{*-}$	0.027	$D^+ \rightarrow \mu^+ \nu_\mu \bar{K}^{*0}$	0.044
$D^0 \rightarrow \mu^+ \nu_\mu \bar{K}^0 \pi^-$	0.002	$D^+ \rightarrow \mu^+ \nu_\mu \bar{K}^0 \pi^0$	0.005
$D^0 \rightarrow \mu^+ \nu_\mu K^- \pi^0$	0.002	$D^+ \rightarrow \mu^+ \nu_\mu K^- \pi^+$	0.032
$D^0 \rightarrow \mu^+ \nu_\mu \bar{K}^{*0} \pi^-$	0.004	$D^+ \rightarrow \mu^+ \nu_\mu \bar{K}^{*0} \pi^0$	0.011
$D^0 \rightarrow \mu^+ \nu_\mu K^{*-} \pi^0$	0.004	$D^+ \rightarrow \mu^+ \nu_\mu K^{*-} \pi^+$	0.011
$D^0 \rightarrow \mu^+ \nu_\mu \pi^-$	0.002	$D^+ \rightarrow \mu^+ \nu_\mu \pi^0$	0.001
$D^0 \rightarrow \mu^+ \nu_\mu \rho^-$	0.002	$D^+ \rightarrow \mu^+ \nu_\mu \eta$	0.001
$\Lambda_c^+ \rightarrow \mu^+ \nu_\mu \Lambda^0$	0.021	$D^+ \rightarrow \mu^+ \nu_\mu \eta'$	0.001
$\Lambda_c^+ \rightarrow \mu^+ \nu_\mu \Sigma^0$	0.005	$D^+ \rightarrow \mu^+ \nu_\mu \rho^0$	0.001
$\Lambda_c^+ \rightarrow \mu^+ \nu_\mu \Sigma^{*0}$	0.005	$D^+ \rightarrow \mu^+ \nu_\mu \omega$	0.001
$\Lambda_c^+ \rightarrow \mu^+ \nu_\mu n$	0.003	$D_s^+ \rightarrow \mu^+ \nu_\mu \eta$	0.025
$\Lambda_c^+ \rightarrow \mu^+ \nu_\mu \Delta^0$	0.002	$D_s^+ \rightarrow \mu^+ \nu_\mu \eta'$	0.008
$\Lambda_c^+ \rightarrow \mu^+ \nu_\mu p^+ \pi^-$	0.006	$D_s^+ \rightarrow \mu^+ \nu_\mu \phi$	0.02
$\Lambda_c^+ \rightarrow \mu^+ \nu_\mu n \pi^0$	0.006	$D_s^+ \rightarrow \mu^+ \nu_\mu K^+ K^-$	0.005
		$D_s^+ \rightarrow \mu^+ \nu_\mu K^0 \bar{K}^0$	0.005

Table 2.2: Muonic branching ratios used in the analysis [32].

If all variables would be known independently, we would be able to calculate the tauonic branching ratio. However, the decay constant f_{D_s} is usually derived from measurements of the purely muonic and tauonic branching ratios (and amounts to $f_{D_s} = 254 \pm 25$ MeV [33]). Therefore, in the following we use the measured value of $B_{D_s \rightarrow \tau \nu_\tau} = 0.07 \pm 0.04$ [5].

2.5 Present experimental status

To study neutrino induced charmed particles, very massive detectors are needed, because of the relatively small neutrino cross section and the presently available neutrino beam intensities. On the other hand charmed particles have a very short lifetime that requires a high spatial resolution for direct detection. Therefore, most of the earlier experiments investigating charm production relied on the measurement of inclusive muonic decays. The most relevant experiments in this field are E531, CCFR and NuTeV at Fermilab, and BEBC, CDHS, CHARM, CHARM II and NOMAD at CERN.

In only two experiments nuclear emulsion was used: at Fermilab by the E531 experiment and at CERN by the CHORUS experiment.

A short summary of the experimental apparatus for each of the experiments is given, before we describe the CHORUS detector in detail in the next chapter.

- E531

In the E531 experiment [34], 23 liters of emulsion are used as primary neutrino target in the Fermilab wide-band neutrino beam. The target is followed by a drift chamber spectrometer with a wide angular acceptance and a time-of-flight (TOF) system equipped with scintillator hodoscopes. Further downstream, a lead-glass calorimeter ($\Delta E/E = 0.14/\sqrt{E}$) is followed by an iron calorimeter ($\Delta E/E = 1.1/\sqrt{E}$) interspersed with scintillator planes. An iron hadron absorber and scintillator planes are installed to identify muons. The experiment is optimized to measure hadronic decays of charmed particles. The momentum resolution of decay tracks is given by $\Delta p = \sqrt{(0.004p^2)^2 + (0.014p)^2}$. The data taking period covers 1978 - 1981.

- CCFR

The most recent results from the CCFR collaboration come from data taken in 1985 and 1987 in the Fermilab wide-band neutrino beam. The detector [35] is constructed as a target calorimeter followed by a toroidal

muon spectrometer. The calorimeter consists of iron plates interspersed with scintillators and drift chambers. The measured energy resolution is $\Delta E/E_{had} = 0.89/\sqrt{E_{had}}$. The muon spectrometer has drift chambers for muon tracking and hodoscopes for triggering. The momentum resolution is $\Delta p/p = 0.11$.

- NuTeV

The NuTeV experiment [36] took data during the period 1996 - 1999 in the Fermilab wide-band neutrino beam. The detector consists of a target calorimeter followed by a toroid spectrometer. The calorimeter is composed of steel plates acting as target, interspersed with liquid scintillator counters and drift chambers to reconstruct tracks and measure the energy deposition. The hadronic energy resolution of the calorimeter is $\Delta E/E = 0.86/\sqrt{E}$. The spectrometer measures charge and momentum of muons ($p > 5$ GeV) with a resolution $\Delta p/p = 0.11$.

- BEBC

The BEBC experiment took data in the CERN narrow-band and wide-band neutrino beams in the 1970's and 1980's. The cryogenic bubble chamber has a 10 m^3 fiducial volume surrounded by a 3 Tesla superconducting magnet and is supplemented with a two-plane 150 m^2 external muon identification system.

- CHARM

The CHARM experiment [37] took data in the CERN narrow- and wide-band neutrino beam in the early 1980's. The detector is composed of a fine grained calorimeter followed by a muon spectrometer. The calorimeter consists of marble (CaCO_3) plates sandwiched with scintillation counters, proportional drift tubes and streamer tubes. The muon spectrometer consists of an iron toroid spectrometer surrounded by a magnetized iron frame and is instrumented with proportional drift chambers. The hadronic energy resolution is $\Delta E/E_{had} = 0.49/\sqrt{E_{had}}$. The muon momentum resolution $\Delta p/p$ is 0.15 to 0.20 on average.

- CDHS

The CDHS experiment [38] took data in the early 1980's both in the narrow-band and in the wide-band neutrino beams at CERN. It consists of a calorimeter with toroidally magnetized iron plates sandwiched between planes of scintillator planes and drift chambers. Depending on

the interaction vertex with respect to the segmentation, the hadronic energy resolution varies between $\Delta E/E_{had} = 0.58/\sqrt{E_{had}}$ and $\Delta E/E_{had} = 0.70/\sqrt{E_{had}}$. The muon momentum is measured in a magnetic field with an average resolution $\Delta p/p$ of 0.09.

- CHARM II

The CHARM II experiment [39] collected data during the period 1987 - 1991 using the CERN wide-band neutrino beam. The target is composed of glass plates interspersed with streamer tubes and scintillation counters. The electromagnetic energy resolution is $\Delta E/E = 0.09 + 0.15/\sqrt{E}$ and the hadronic energy resolution is $\Delta E/E_{had} = 0.02 + 0.52/\sqrt{E_{had}}$. The target is followed by a muon spectrometer with a resolution $\Delta p/p = 0.13$ at 20 GeV.

- NOMAD

The NOMAD detector [40], located behind the CHORUS detector in the CERN wide-band neutrino beam, consists of a 2.7 ton active drift chamber target, a transition radiation detector, a pre-shower calorimeter ($\Delta E/E = 1.0/\sqrt{E}$), and an electromagnetic calorimeter ($\Delta E/E = 0.01 + 0.032/\sqrt{E}$), all located inside a dipole magnetic field of 0.4 T. Installed outside the magnetic field is an iron-scintillator hadronic calorimeter ($\Delta E/E = 1.0/\sqrt{E}$) followed by steel absorbers instrumented with drift chambers for detection and tracking of muons. The muon momentum resolution is $\Delta p/p = 0.03$ for momenta below 20 GeV. Data taking took place in the period 1994 - 1998.

From the point of view of charm physics the experiments mentioned above contributed to measurements of the charm production cross section (relative to the full CC cross section), the charm quark mass, the strange sea and the charm fragmentation function. Details of the results from the other experiments are given in the relevant sections of the analysis chapters.

Before CHORUS the E531 experiment was the only detector allowing direct detection and reconstruction of hadronic charm decays. Therefore, it could provide the relative production rates of the different charmed particle types, which lead to the first, and until this work only, direct measurement of the CKM matrix element V_{cd} [17].

Concerning diffractive D_s production two results are available. One result combines all available experimental bubble chamber data [41], and recently the

The separation varied with respect to the experimental set-up with the
 (24) method. It consisted of two stages: first, a separation of the
 very high energy events (above 100 GeV) and a second stage of
 separation of the low energy events (below 100 GeV) with respect to the
 detector set-up. The main detector is composed of a magnetic field
 of about 1.5 T, a calorimeter, a counter and a detector set-up which has
 an energy resolution of 10% at 100 GeV.

CHARM II experiment has been designed to measure a number of charm
 production cross-sections. The CHARM II experiment is composed of two stages: first, a separation of the
 very high energy events (above 100 GeV) and a second stage of
 separation of the low energy events (below 100 GeV) with respect to the
 detector set-up. The main detector is composed of a magnetic field
 of about 1.5 T, a calorimeter, a counter and a detector set-up which has
 an energy resolution of 10% at 100 GeV. The target is followed by a
 calorimeter with a resolution of 10% at 100 GeV.

• **HOMED**

The HOMED detector is designed to measure charm production in
 the CHARM wide-angle window. It consists of a 1.7 m radius drift
 chamber (large x -projection) and a 1.7 m radius drift chamber (small
 x -projection) with a resolution of 10% at 100 GeV. The calorimeter
 has a resolution of 10% at 100 GeV. The calorimeter is composed of
 a lead calorimeter (large x -projection) and a lead calorimeter (small
 x -projection) with a resolution of 10% at 100 GeV. The calorimeter
 is composed of a lead calorimeter (large x -projection) and a lead
 calorimeter (small x -projection) with a resolution of 10% at 100 GeV.
 The calorimeter is composed of a lead calorimeter (large x -projection)
 and a lead calorimeter (small x -projection) with a resolution of 10%
 at 100 GeV. The calorimeter is composed of a lead calorimeter (large
 x -projection) and a lead calorimeter (small x -projection) with a
 resolution of 10% at 100 GeV. The calorimeter is composed of a
 lead calorimeter (large x -projection) and a lead calorimeter (small
 x -projection) with a resolution of 10% at 100 GeV. The calorimeter
 is composed of a lead calorimeter (large x -projection) and a lead
 calorimeter (small x -projection) with a resolution of 10% at 100 GeV.

From the point of view of these proposed experiments mentioned above
 contributed to measurements of the charm production cross-sections (higher to
 the full CC cross-section), for that is worth noting the progress and the charm
 fragmentation function. Details of the results from the other experiments are
 given in the previous sections of this chapter.

Before CHORUS the EMI experiments were the only detector offering direct
 detection and reconstruction of hadronic-charm decays. Therefore, it could
 provide the relative production rates of the different charged particle types,
 which lead to the d/s and u/s ratios only. Direct measurement of the
 CKM matrix element V_{cb} [17].

Concerning distinctive D_c production, the results are available. Our most
 complete all available experimental results (see Table 2.1) and remain the

Chapter 3

The CHORUS experiment

Magic is any sufficiently advanced technology.
Arthur C. Clarke [43]

The CHORUS (CERN Hybrid Oscillation Research Apparatus) experiment has been designed to search for neutrino oscillations of the type $\nu_\mu \rightarrow \nu_\tau$. It aims primarily at the detection of ν_τ induced charged current interactions $\nu_\tau N \rightarrow \tau^- X$. Due to the short lifetime of the τ lepton ($c\tau \sim 90 \mu\text{m}$) excellent spatial resolution is needed. Therefore, nuclear emulsion is used simultaneously as a neutrino target and as a tracker in three dimensions with sub- μm resolution. It allows to examine the primary interaction vertex along with any short-lived particle decay. In this thesis, we report on a study of the production and decay of - also very short lived - charmed particles.

The topology and kinematics of the neutrino events are obtained by combining data from the electronic detector with tracks measured in the integrating emulsion detector (*hybrid setup*). The electronic detector information is used to predict the particle trajectories in the emulsion. Automated microscopes follow these trajectories through the emulsion until a primary neutrino interaction is found.

To match electronic detector tracks with emulsion tracks, the emulsion is interspersed with layers of high resolution scintillating fiber trackers. For the kinematic reconstruction, downstream of this target area a hadron spectrometer, a calorimeter and a muon spectrometer are situated. The detector is schematically shown in Figure 3.1.

The CHORUS experiment took data with emulsion target in the period 1994 - 1997. In 1998 neutrino and anti-neutrino data were taken for calibra-

tion purposes and for dedicated studies, in particular for a structure function measurement using the calorimeter as target [44].

In this chapter we describe the main points of the neutrino beamline, the CHORUS subdetectors relevant for our work, and the properties, handling and scanning of the emulsion target. A complete and detailed description of the experimental setup can be found in Reference [45].

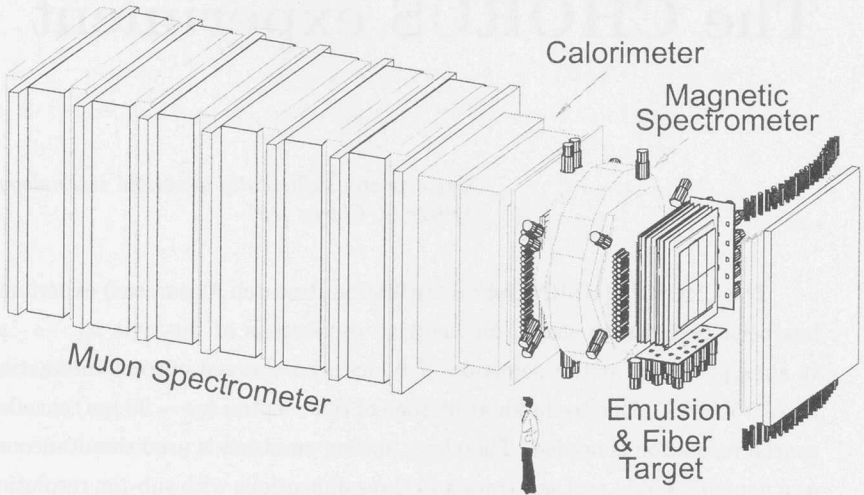


Figure 3.1: The CHORUS detector.

3.1 Neutrino beam

The CHORUS experimental setup has been installed in the beamline of the West Area Neutrino Facility (WANF), which was operated in the wide band mode [46, 47]. The layout of the beam line is shown in Figure 3.2.

Protons are accelerated with the Super Proton Synchrotron (SPS) to 450 GeV in a cycle of 14.4 s. They are extracted in two 6 ms long spills, separated in time by 2.7 s, and then stopped in a beryllium target producing mainly pions and kaons. For the neutrino beam a sophisticated setup of pulsed magnetic lenses (horn and reflector) focuses the positively charged mesons while the negatively charged mesons are bent out of the beamline. The mesons decay in flight in a 290 m long evacuated tunnel and produce neutrinos mainly via the decay

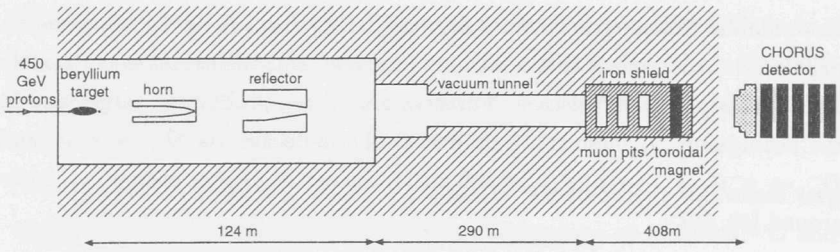


Figure 3.2: Schematic overview of the neutrino beamline WANF (not to scale).

channels

$$\begin{aligned}
 \pi^+ &\rightarrow \mu^+ \nu_\mu, \\
 K^+ &\rightarrow \mu^+ \nu_\mu, \\
 K^+ &\rightarrow \pi^0 \mu^+ \nu_\mu.
 \end{aligned}
 \tag{3.1}$$

The charged leptons from the decay as well as the remaining not-decayed mesons are absorbed in a beamdump of iron and a 400 m long path through earth.

For the whole neutrino beamline a Monte-Carlo (MC) simulation has been developed (GBEAM [48]). The resulting energy spectra of the *wide-band* beam composition - consistent with measurements [44] - are displayed in Figure 3.3.

The neutrino beam consists mainly of muon neutrinos with a mean energy $\langle E_{\nu_\mu} \rangle = 27$ GeV. Contamination with other (anti-)neutrino flavours is

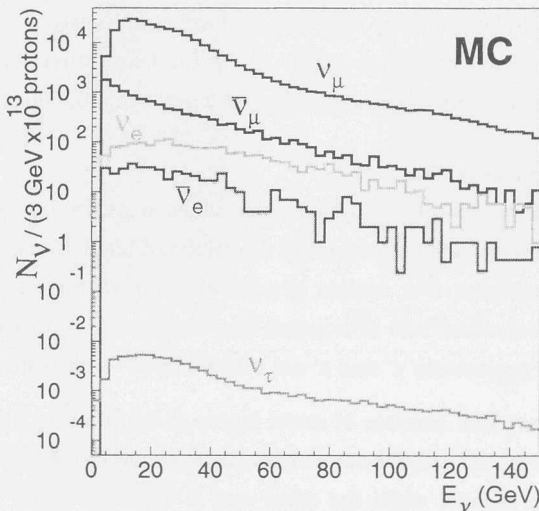


Figure 3.3: The neutrino spectrum in the CHORUS experiment.

unavoidable. Muon anti-neutrinos primarily result from K^0 decays and the remaining π^- component in the beam. Electron (anti-)neutrinos come mainly from semi-leptonic K^\pm decays. Furthermore, in the production target and in the beamdump D_s mesons are produced. Their decays via $D_s^+ \rightarrow \tau^+ \nu_\tau$ and $D_s^- \rightarrow \tau^- \bar{\nu}_\tau$, $\tau^- \rightarrow \mu^- \bar{\nu}_\mu \nu_\tau$ result in an almost negligible prompt ν_τ background [49, 50].

3.2 The experimental setup

3.2.1 Target area

In the target area, stacks of nuclear emulsion and scintillating fiber trackers are installed:

- **Emulsion [51]**

A volume of 206 liters nuclear emulsion, in total weighing 770 kg, is used in CHORUS for two purposes: as '*bulk sheets*' in the primary neutrino target and as '*changeable (CS) and special sheets (SS)*' for high precision tracking to interlink the electronic trackers and the bulk emulsion.

The bulk emulsion is distributed over 4 stacks, each consisting of eight modules with a size of $0.36 \times 0.72 \text{ m}^2$ installed on aluminium frames, and covering in total an area of $1.42 \times 1.44 \text{ m}^2$. Each module consists of 36 individual plates. Every plate has a $90 \mu\text{m}$ thick plastic base covered with $350 \mu\text{m}$ emulsion on both sides. Along the beam direction, the installed emulsion amounts to about 4 radiation lengths and 0.3 interaction lengths.

- **Fiber trackers [52]**

Fiber trackers are placed between the emulsion stacks to predict exit points from the upstream emulsion and directions of particle trajectories. Every tracker contains four tracker planes, allowing to measure unambiguous track parameters from orthogonal small-angle stereo projections (y, z, y', z'). The projections y' and z' are rotated by 8° with respect to y and z .

A tracker plane consists of seven layers of scintillating fibers. The fiber diameter is $500 \mu\text{m}$. One end of the fibers is covered with aluminium that acts as a mirror, while the other end is attached to an opto-electronic chain with a CCD camera. In total one million fibers are connected to 58 opto-electronic readout chains.

The achievable precision in track reconstruction increases successively in the upstream direction from the fiber trackers ($150 \times 150 \mu\text{m}^2$) to the bulk emulsion plates ($10 \times 10 \mu\text{m}^2$). The angular precision for the fiber tracker is about 2 mrad, and 1.5 mrad in the emulsion.

To reduce fading of the latent images in the emulsion, the whole target region is inside a coolbox and kept at a temperature of $(5.0 \pm 0.5)^\circ \text{C}$ and a relative humidity of 60%.

Since the neutrino interaction probability is proportional to the amount of traversed mass, we can inspect the detector by *neutrino tomography*. The distribution of (target) material can be seen in Figures 3.4, where all reconstructed neutrino interaction vertices from data taken in the period 1994 - 1997 are plotted in the longitudinal and the transverse projections.

In the neutrino tomography image of the longitudinal projection the distribution of emulsion stacks and fiber tracker planes is visible. Furthermore, between -70 cm and -50 cm the presence of a pilot fiber target setup [53] can be seen. In the transverse projection the small gaps showing the aluminum frame holders between the eight emulsion modules are just visible.

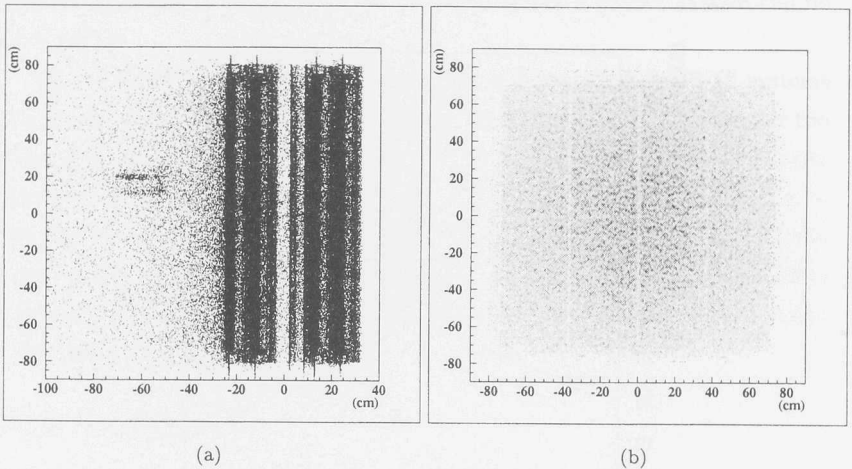


Figure 3.4: Neutrino tomography image of the target area in longitudinal (a) and transverse (b) projection.

3.2.2 Hadron spectrometer

An air-core magnet [54] with a hexagonal shape is used for momentum and charge determination of charged particles (particularly hadrons) emerging from the target area. The magnet produces a toroidal field of 0.12 T and it is pulsed synchronously with the neutrino beam.

In front of the magnet and behind, planes of scintillating fiber trackers are installed to measure the trajectory curvature. To reach even higher precision of trajectory parameters, an emulsion tracker (ET) has been installed inside the magnet before the 1996 run.

The momentum resolution is the quadratic sum of two parts: (a) uncertainties of the track parameters before and after traversing the magnet

$$\frac{\Delta p}{p_{meas.}} = 3.5\% \times p/\text{GeV}; \quad (3.2)$$

and (b) the momentum independent error due to multiple scattering inside the magnet

$$\frac{\Delta p}{p_{scatt.}} = 22\%. \quad (3.3)$$

The momentum resolution of the spectrometer as a function of the momentum is depicted for muons in Figure 3.5.

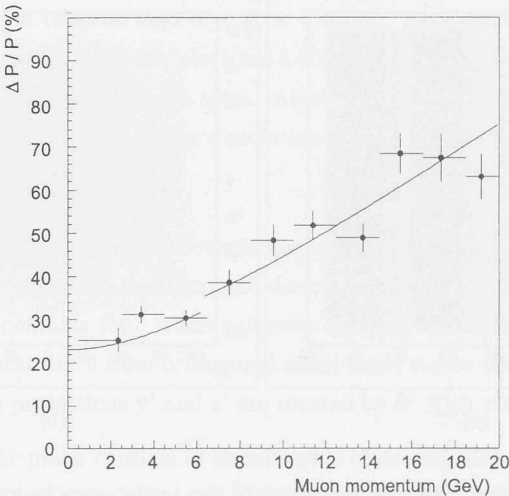


Figure 3.5: The muon momentum resolution for the hexagonal magnet spectrometer.

3.2.3 Honeycomb chamber

A honeycomb tracker has been installed during the 1996 run to improve the track matching between the hexagonal magnet and the calorimeter.

The tracker planes are built-up from hexagonal cells, where each cell is acting as a single wire drift chamber. The position of passing-through charged particle trajectories is extracted by measuring the drift time of the ionization electrons. The tracker consists of 3 modules of 6 planes ($\sim 3 \times 3 m^2$) at angles of 0° and $\pm 60^\circ$ with respect to the horizontal Y-axis. The obtained residual after alignment and calibration is typically about $300 \mu\text{m}$.

Rasnik alignment system

In 1996 three RASNIK systems (Relative Alignment System of NIKhef) have been installed to monitor the relative alignment of the honeycomb chambers (a fourth system has been installed to monitor the alignment of the hadron spectrometer).

The basic principle of the RASNIK is to project a coded mask - a finely detailed image ($85 \mu\text{m}$ black-and-white squares on a raster) - through a lens onto a CCD camera. When the image of the mask moves, the local displacement is measured with a precision of a few μm . The pattern is used to decode the global position information. More details of the setup of the RASNIK system can be found in [55].

Figure 3.6 shows the movements registered with one of the RASNIK systems for a one month period in 1997 data taking. The upper two plots represent the lateral movements, whereas the lower plot shows the longitudinal movement (which is less precisely determined). The maxima and minima correspond to daily changes of the temperatures. In the substructure of the curves, the cycle of the ventilation system is just visible. Indicated in the figure are movements larger than the daily changes that could be correlated with manual interventions in the experimental area.

3.2.4 Calorimeter

It is important to measure the energy and to some extent also the direction and other characteristics of electromagnetic and hadronic showers emerging directly or indirectly from a neutrino interaction in the target. This is done in the calorimeter which has three segments with different granularity and dimensions. One segment (EM) is primarily sensitive to the electromagnetic component of

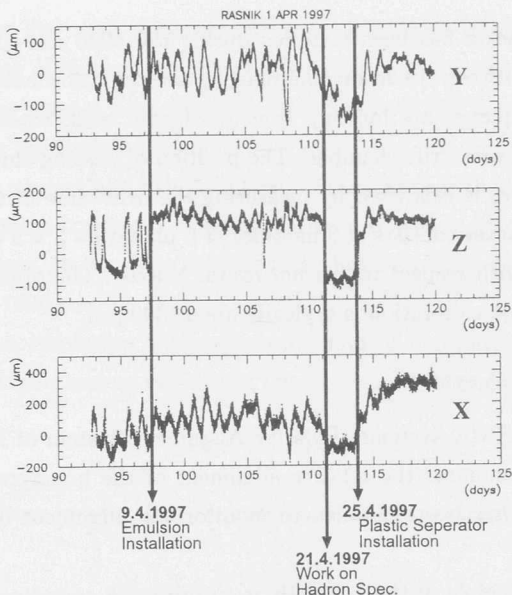


Figure 3.6: A one month record of movements along the three axes measured by one honeycomb chamber RASNIK system.

showers and two segments (HAD1 and HAD2) to the hadronic part.

The modules EM and HAD1 have been built using a 'spaghetti' technique [56], where scintillating fibers (1 mm diameter) are embedded in a lead matrix. In HAD2, lead plates (16 mm thickness) are interspersed with scintillator strips (4 mm thickness). Between the calorimeter modules streamer tubes are mounted to get tracking information, in particular concerning muons. Details on the construction of the calorimeter can be found in Reference [57].

The volume ratio between lead and scintillator is 4:1 to reach an optimal compensation of the differences in detector response for electromagnetic and hadronic showers. This provides a good resolution for the measured total shower energy. The total thickness of the calorimeter corresponds to about 150 radiation lengths or 5.6 hadronic interaction lengths.

The energy resolution for electrons and pions is shown in Figure 3.7. For electrons it can be parameterized as

$$\frac{\Delta E}{E} = \frac{(13.8 \pm 0.9)\%}{\sqrt{E \text{ (GeV)}}} + (-0.2 \pm 0.4)\%, \quad (3.4)$$

and for pions as

$$\frac{\Delta E}{E} = \frac{(32.3 \pm 2.4)\%}{\sqrt{E \text{ (GeV)}}} + (1.4 \pm 0.7)\%. \quad (3.5)$$

Details on the measured performance of the calorimeter can be found in Reference [58].

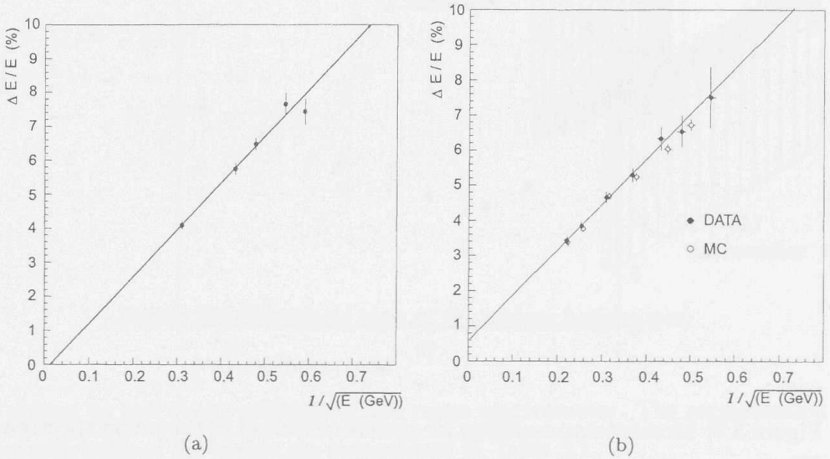


Figure 3.7: Measured energy resolution of the calorimeter for electrons (a) and pions (b), in the latter case compared with Monte-Carlo predictions. The solid straight lines represent the resolution function resulting from a fit to the data points.

3.2.5 Muon spectrometer

In the muon spectrometer, situated downstream directly behind the calorimeter, the momentum and charge sign of muons are determined. The calorimeter stops nearly all particles, except muons with a momentum greater than 1.5 GeV. The spectrometer is built-up from six toroidally magnetized iron disk modules (375 cm in diameter) sandwiched by seven tracking units with streamer tubes and drift chambers. The drift chamber modules are installed under 0° and $\pm 60^\circ$ with respect to the horizontal Y-axis.

Embedded in the iron disks are scintillation counters primarily delivering a muon trigger signal. In addition, a range measurement and thus a momentum determination of muons with a momentum of less than 5 GeV at the entrance to the spectrometer is possible.

The momentum resolution of the muon spectrometer is shown in Figure 3.8.

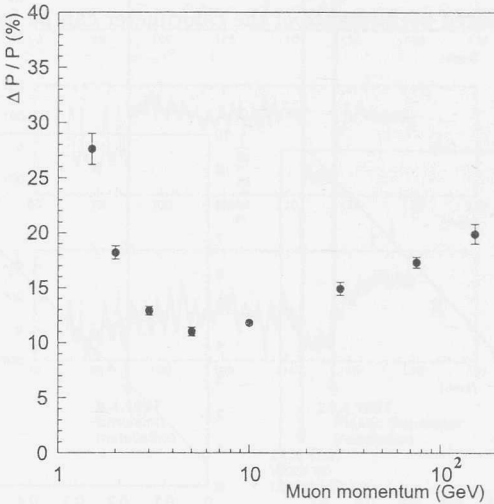


Figure 3.8: Momentum resolution for muons measured in the muon spectrometer.

3.2.6 Trigger system

The trigger system has been designed to primarily select neutrino induced interactions in the emulsion target and to reject background from cosmic rays, beam muons and neutrino interactions outside the target. In Figure 3.9 the setup of the scintillator hodoscopes (E, T, H, V and A) is shown. The E and T planes are installed between the emulsion target and hadron spectrometer, whereas H is located downstream of the hadron spectrometer. The A and V planes are installed upstream of the emulsion target. The size of the V plane has been chosen to fully cover the area defined by the angular acceptance of the E, T and

Plane	A	V	E	T	H
Strips/layer	16	20	7	15	20
Strip width (cm)	20	20	20	10	10
Strip length (cm)	200	320	148	160	200
Orientation	vert.	vert.	vert.	hor.	hor.
Area covered(cm ²)	200 × 320	400 × 320	150 × 148	160 × 160	200 × 200

Table 3.1: Segmentation characteristics of trigger hodoscopes.

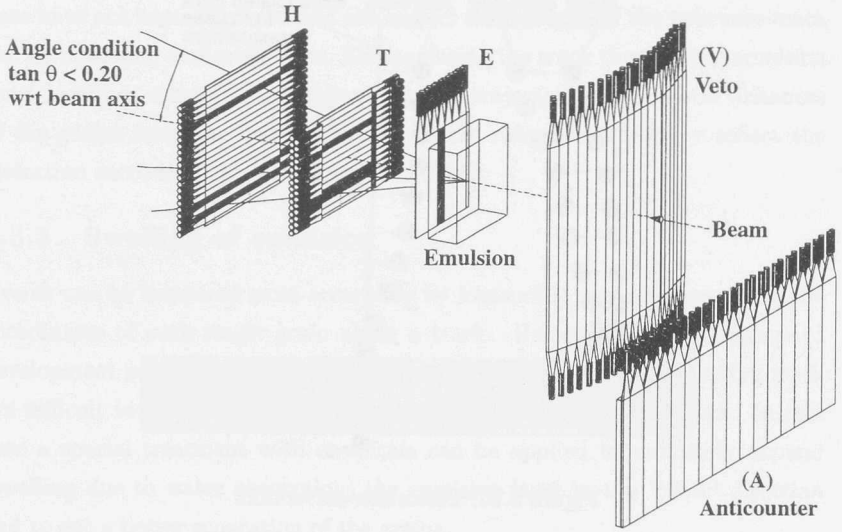


Figure 3.9: Schematic view of the trigger hodoscopes.

H planes, as well as the calorimeter and muon spectrometer. The segmentation characteristics of the planes are summarized in Table 3.1.

A neutrino trigger in the target region is defined by a coincidence of hits in the hodoscopes E, T and H consistent with a particle trajectory with $\tan \theta < 0.20$ with respect to the neutrino beam axis. A veto is formed by any combination of a counter hit in the veto hodoscopes (V and A). Precise timing between T and V is needed (2 ns FWHM) to avoid vetoes due to backscattering of particles coming from neutrino interactions in the target. The trigger efficiency is typically 99%. Details of the trigger system can be found in Reference [59].

3.3 Emulsion target

Using nuclear emulsion for visualizing particle trajectories is an old technique. In fact, many particles (π^+ , π^- , π^0 , K^+ , K^- , Σ^+ , $\bar{\Lambda}$ [60]) have been discovered with nuclear emulsion as a detector. Modern emulsion detectors are still based on the same principle, but their performance, ease of handling and their scanning have been improved tremendously. In this section, the emulsion handling and scanning is summarized, while including specific details relevant for the work described here.

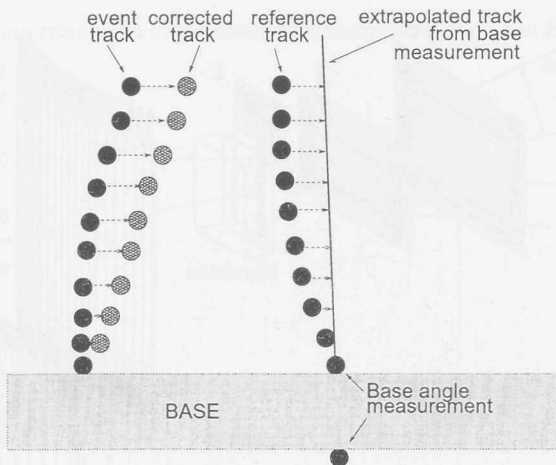


Figure 3.10: Distortion correction.

3.3.1 Track formation

Along their path through the emulsion, charged particles break the bonds of silver-bromide molecules. The bromide diffuses slowly outward and along the particle trajectory specks of metallic silver remain behind. During the exposure those specks are not visible, they form a latent track image. The specks serve as active centers during the development process at a later stage. After subsequent chemical fixing and drying of the emulsion, grains of metallic silver form a visible track along the trajectory of any ionizing particle having passed through.

3.3.2 Emulsion shrinkage and track distortion

After the development and fixation, the CHORUS emulsion has shrunk by a factor of typically 1.9. This shrinkage factor is locally constant. After the development, emulsion is still hygroscopic so that the equilibrium thickness depends on the ambient humidity and temperature. Therefore, scanning and storage of emulsion plates requires controlled environmental conditions.

In the preparation phase, processing the emulsion generates inherent stresses that - after development - result in a gradual non-linear lateral displacement of the emulsion, increasing from the plastic base to the surface. Tracks are thus distorted in the emulsion. The distortion factor is locally constant and can be derived from arbitrary straight through-going reference tracks nearby (Figure 3.10). Since the emulsion is fixed on the plastic base, grains close to the

base have not been displaced and the correct track angles of the reference track can be measured across the base. Extrapolating the track through the emulsion then describes correctly the original particle trajectory. The lateral distances of the grains from the measured track to the reference trajectory reflect the distortion correction as a function of the depth.

3.3.3 Swelling of emulsion

Events can be measured most accurately by measuring in three dimensions the coordinates of each single grain along a track. However, after the standard development procedure subsequent silver grains belonging to a traversing track are difficult to be resolved under a microscope due to the focal depth. In this case a special treatment with chemicals can be applied to uniformly expand (swelling due to water absorption) the emulsion layer in the 'beam' direction and to get a better separation of the grains.

Procedure 1	Temperature	Time	Purpose
water	23.5°C	4h	slow expansion
cooling	5°C	1h	
CH ₃ COOH	5°C	2h	fast expansion
Na ₂ SO ₄	23.5°C	24h	stop expansion
D-sorbitol + glycerin + water (0.823:0.144:1)	23.5°C	24h	fixing
Procedure 2	Temperature	Time	Purpose
water	23.5°C	4h	slow expansion
cooling	5°C	1h	
CH ₃ COOH	5°C	2h	fast expansion
Na ₂ SO ₄	23.5°C	24h	stop expansion
alcohol (60%) + glycerin (25%) + water (15%)	23.5°C	24h	fixing
Procedure 3	Temperature	Time	Purpose
water	19°C	10h	slow expansion
alcohol (50%) + glycerin (50%)	19°C	22h	stop expansion and fix

Table 3.2: Procedures for emulsion swelling.

This technique has been applied for the special event presented in Chapter 5. Several tests have been performed with a series of test emulsion plates using different procedures and chemicals. Plates were hung in a basin filled with a specific test solution, while kept under constant temperature. In this way a uniform expansion was obtained. Different trials are listed in Table 3.2. Procedure 3 has been chosen to be applied on the CHORUS emulsion plate

containing the above mentioned event. Procedure 2 was abandoned because the expansion rate was too small. The plates treated with procedure 1 showed a proper expansion, however sorbitol crystallized and damaged the surface of the emulsion after drying.

3.3.4 Automatic scanning

Until approximately 10 years ago, emulsion could be read out exclusively by manually controlled microscopes. However, analyzing the CHORUS emulsion manually would take hundreds of man-years. The CHORUS experiment is only possible thanks to the development of automatic scanning systems [61].

Using track predictions from the target tracker, automated microscope systems controlled entirely by computers locate in good approximation the corresponding tracks in the emulsion. A CCD camera takes images at different depths resulting in a tomographic digital representation of the emulsion. Using automatic control, identified particle trajectories are then traced backward through the emulsion plates until the primary vertex is found.

The technique for automatic scanning has been pioneered by the Nagoya-University group [61]. Recently the CERN and NIKHEF groups have jointly

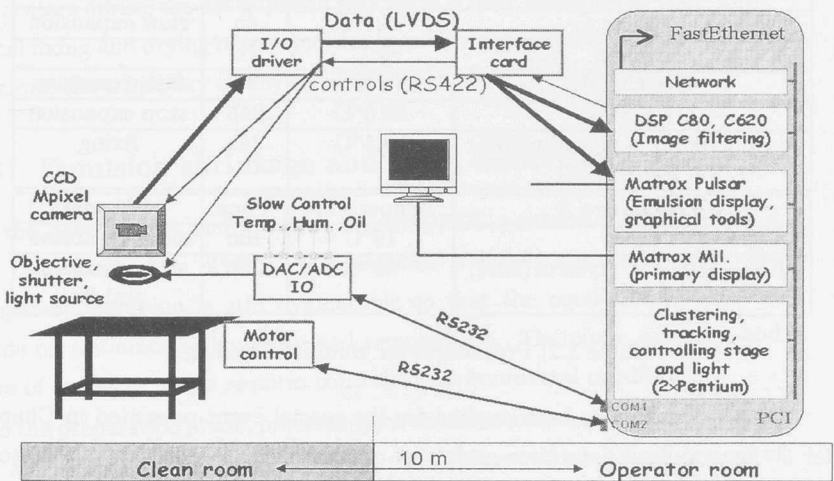


Figure 3.11: Schematic description of the track recognition by an automatic scanning system (see text).

set up a laboratory for automatic emulsion scanning at CERN [62].

In the Nagoya-setup tracks are recognized by hardware controlled summing of the binary images while applying a differential shift corresponding to the predicted track angles. At the correct differential shift a track shows up as a pronounced peak or cluster in the summed image.

In the CERN/NIKHEF-setup a software controlled, and thus more flexible track detection method has been implemented. The CCD-images are first digitally filtered to enhance the grain signal. The barycentres of pixel clusters over threshold are then used as grain coordinates. From these three-dimensional coordinates (about 3000 per layer) the particle trajectories are reconstructed.

A schematic description of the CERN/NIKHEF scanning station¹ is given in Figure 3.11. A digital CCD camera² (1024×1024 pixels, 15-30Hz) reads the images from the microscope optics.³ The online data taking is controlled by a personal computer (PC) equipped with a digital signal processor (DSP) board.⁴ Apart from filtering and identifying grains, the DSP is also used to control the camera and the shutter of the optics. Microscope tables⁵ (800×400 mm²) are positioned with micro-stepper motors via the serial interface of the PC. The compressed grain data (19 bits/grain) are sent via fast 100 MB/s ethernet to a cluster of dual Pentium III machines, where the tracking is performed. Results from the data taking are stored in an Objectivity database running on a SUN Sparc5. Environmental conditions are not only controlled but also monitored and stored in the database. For physics analysis, the most relevant data that need fast access (e.g. reconstructed tracks) are stored on 300 GB of RAID disks. For the low level data (raw images) 1 TB tape space on the High Performance Storage System (HPSS) system at CERN has been allocated. Four scanning stations (3 CERN, 1 NIKHEF) have been equipped with the described set-up.

Other scanning laboratories contributing to the CHORUS analysis are located in the universities of Ankara, Bari, Naples, Rome, Salerno, Toho and Utsunomiya.

3.3.5 Scanning procedure

The scanning starts with a given target tracker (TT) track, whose corresponding emulsion track is searched with the automatic microscope in the *CS* plate.

¹Status: Autumn 1999

²manufactured by Thomson [63]

³manufactured by Jenoptik [64]

⁴manufactured by LSI/Blue Wave [65]

⁵manufactured by MICOS [66]

The scanning is done by spiraling outward around the predicted position and searching for trajectories in the emulsion with similar direction (in the following also called *angle*) as the TT track. The spiraling stops as soon as a candidate has an angle in the emulsion differing by $\Delta\theta < 6$ mrad from the predicted direction. If no such match is found, all candidates in the area of 11×11 microscope views (1 view = $120 \times 90 \mu\text{m}^2$ at $50\times$ magnification) with $\Delta\theta < 15$ mrad are denoted as 'found on CS'.

Such a track found on *CS* is then followed on *SS* (see Subsection 3.2.1), using the position found in *CS*. It is searched within 7×7 microscope views centered around the prediction and is called 'found on SS' if its angle differs by less than 15 mrad from the prediction. The measured *SS* angle becomes the reference for the scanning of the target emulsion.

Starting at the back-end of the target emulsion, the initially scanned region is centered around the predicted position and has a radius of $15 + 50 \times \Delta\theta_{X7} \mu\text{m}$.⁶

The angular tolerance for confirming a track is $25 + 50 \times \Delta\theta_{X7}$ mrad. The confirmed tracks are then subsequently followed to the next plate. In the bulk of the emulsion target the plate-to-plate finding efficiency as a function of the track angle is shown in Figure 3.12.

If - during scan-back - no continuation of a track is found in two subsequent plates, the first plate missing the track is called *vertex plate* and the event is denoted for this analysis as having its vertex *located* in the emulsion.

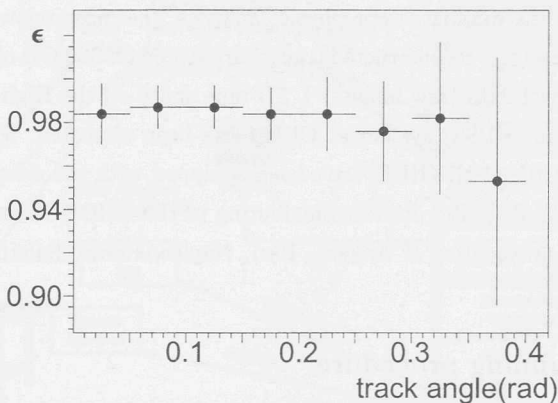


Figure 3.12: The plate-to-plate matching efficiency in the *bulk* emulsion as function of the track angle.

⁶ $\Delta\theta_{X7}$ is the angle with respect to the direction of the X7 testbeam in the CERN West Area. The muon halo of this beam reaches the emulsion target and provides a controlled density of reference tracks in the emulsion.

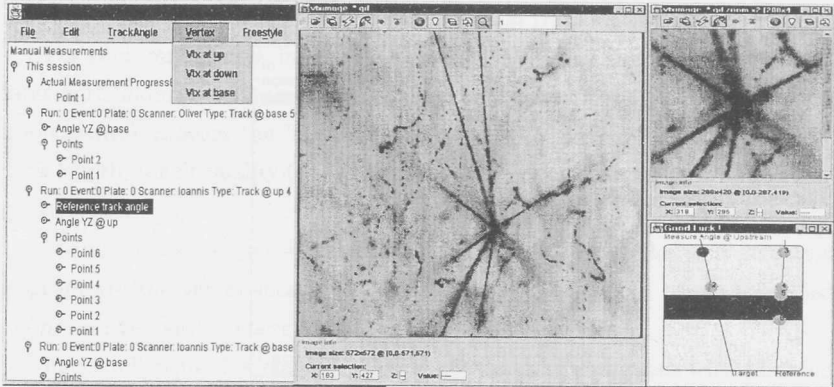


Figure 3.13: Screen-shot of the manual scanning program.

3.3.6 Manual scanning

Once a charm (or τ) candidate vertex has been located by the automatic system, it is checked and measured extensively under manual control. To measure track directions in the emulsion not only sufficiently accurately but also efficiently in time, usually not all grain coordinates along the track are measured and included in the final fit.

If the track crosses the plastic base, the entry and exit grains are measured to simply determine the local track angle. If the track has to be measured inside the emulsion layer, a distortion correction is needed using a reference track (see Subsection 3.3.2).

A screen view of the program implementing decision logics and microscope control for manual measurements on the CERN-NIKHEF scanning stations, is displayed in Figure 3.13.

The accuracy of the manual measurement depends not only on the optical system and emulsion quality, but also on the experience of the scanner. Figure 3.14 shows the difference of the manually measured angles with respect to the automatically measured angles on a special sheet (SS)

$$\Delta\phi = \sqrt{(\theta_{manual}^Y - \theta_{SS}^Y)^2 + (\theta_{manual}^Z - \theta_{SS}^Z)^2}. \quad (3.6)$$

The inaccuracy of a standard manual track angle measurement can therefore be up to 25 mrad. This has to be taken into account in the minimum visible decay angle (see Section 4.1.2).

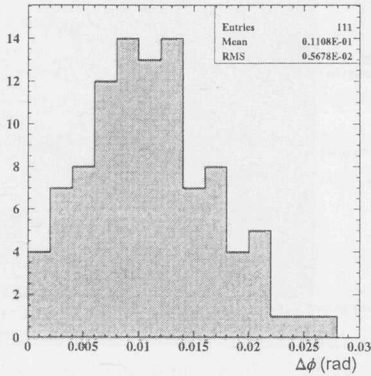


Figure 3.14: Accuracy of the manual track angle measurement.

3.4 Event reconstruction

Signals of the electronic subdetectors are recorded as 'raw' data. Over the running period of one year they amount to about 400 GB. Event reconstruction starts from the raw data using the reconstruction and analysis package CHORAL [67]. The reconstruction output of an event gives access to information that can be used for the analysis.

Inside CHORAL, algorithms perform 'stand-alone' track finding in all subdetectors. Trajectories are then matched between different subdetectors, before the ones emerging from the target region are used to *predict* the track inside the emulsion target.

To find and identify muon tracks in the muon spectrometer and determine their momentum and charge sign, different methods are implemented in the CHORAL package. The SAMTRA method is based exclusively on the drift chamber information while the DATSPC method uses streamer chamber data - both wire and strip hits - as well.

The momentum fitting part of SAMTRA uses a global fit along the length of the track, taking into account the energy loss and multiple scattering [68, 69] in iron and scintillators. Another method, SUPERSAMTRA, uses the DATSPC information with the corresponding driftchamber hits together with the SAMTRA momentum fitting part to obtain the momentum value. For muons in the low momentum range (< 5 GeV) the CAMMOR method is applied to determine the stopping range [70] inside the spectrometer, allowing to derive

the momentum through the range-energy relation [71].

For each muon track in every event there are usually several track candidates with momentum values and charge sign (except for CAMMOR). A decision routine chooses the 'best' result, taking into account the reconstructed track length, the fit quality (χ^2) and whether the muon stopped inside the muon spectrometer.

For our work, the most relevant output parameters of the reconstruction program are the vertex location, the direction and momenta of the identified muons and the visible energy in the calorimeter.

In the following this 'electronic' information will be combined with emulsion information (*hybrid* analysis) to gain insight in charmed particle production.

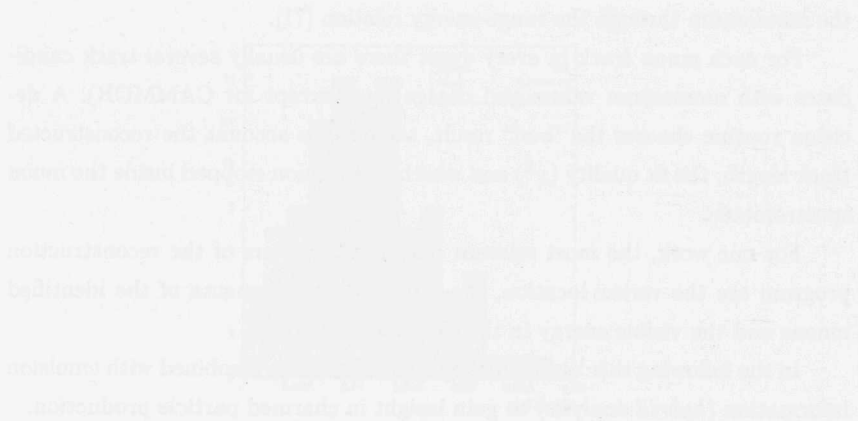


Figure 3.14: Accuracy of the unusual track angle measurement.

3.4 Event reconstruction

Signals of the electronic subsystems are digitized on-line during the running period of one year; they amount to about 220 Tbit. Data reconstruction starts from the raw data using the reconstruction package CHORAL [57]. The reconstruction output of the event reconstruction is a list of tracks that can be used for the analysis.

Inside CHORAL, signal hit patterns are identified and track patterns are reconstructed. Trajectories are then matched between different signal patterns, and the data emerging from the target region are used to produce the track trajectory outside the target.

To find and identify track trajectories the main spectrometer and detector track momenta and charge sign, different methods are implemented in the CHORAL package. The SAMTRA method is based on trajectory on the drift chamber information while the DAIRFC method uses trajectory diameter data, both $+$ -bit and strip hit $-$ -bit rail.

The reconstruction using part of SAMTRA uses a global fit along the length of the track, taking into account the energy loss and multiple scattering [58, 59]. The fit is a minimum χ^2 fit. Another method, SUPERSAMTRA, uses the DAT-500 information with the corresponding drift chamber hit together with the SAMTRA information using part to obtain the momenta values. For momenta in the 100 MeV to 5 GeV range the CAMBION method is applied to determine the tracking angle θ by using the spectrometer, allowing to derive

Chapter 4

Deep inelastic charm production

Neutrino physics is largely an art of learning a great deal by observing nothing.
Haim Harari [72]

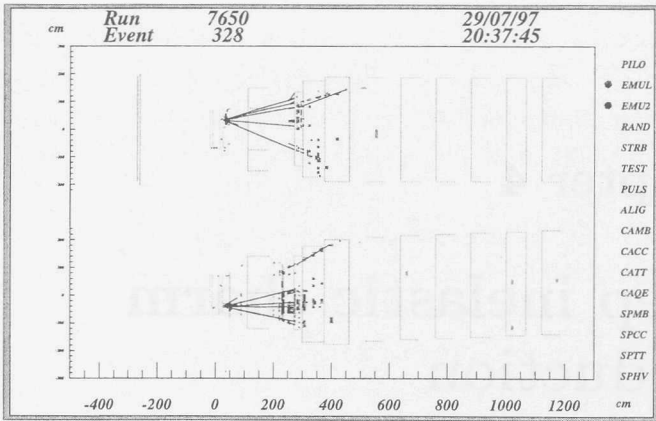
In this chapter the procedure for analyzing charm events produced in charged-current (CC) deep inelastic scattering (DIS) is described and the results are reported. First an introduction is given about the classification and signature of neutrino events in the CHORUS detector. Then the general procedure for the analysis chain of charm events found in the emulsion is described. In order to extract physics results it is necessary to model and understand the data in a Monte-Carlo (MC) simulation. The outcome of the comparison of MC simulation and data is shown and the description of the selection criteria for charm events is presented.

The observed event sample is summarized in terms of event topologies and kinematics. Furthermore, the charm production cross section, the charm quark mass, charm fragmentation, the strange sea component and the weak mixing angle V_{cd} are extracted.

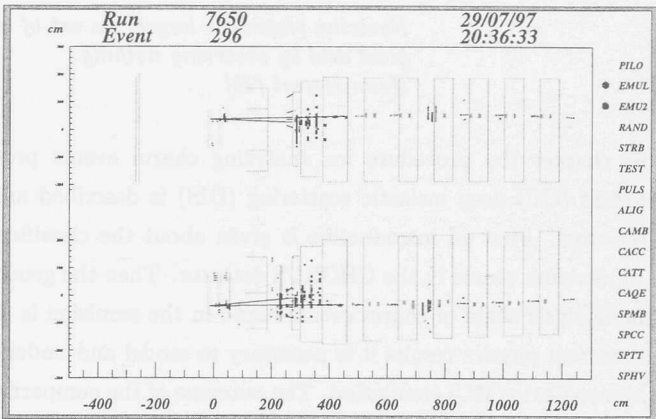
4.1 Analysis procedure

4.1.1 Classification of neutrino events

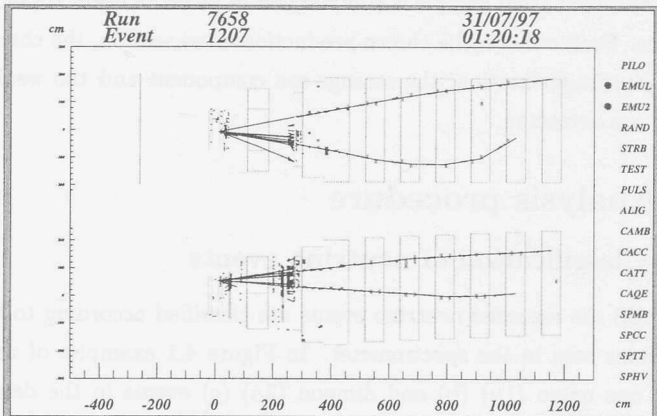
In CHORUS the recorded neutrino events are classified according to the number of muons seen in the spectrometer. In Figure 4.1 examples of zero muon (0μ) (a), one muon (1μ) (b) and dimuon (2μ) (c) events in the detector are



(a)



(b)



(c)

Figure 4.1: Examples of zero, one and two muon events in the CHORUS detector (from top to bottom).

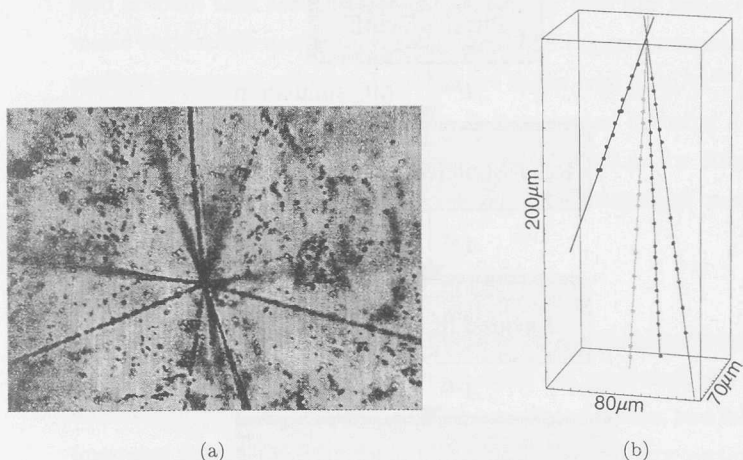


Figure 4.2: A typical neutrino interaction in emulsion (a), and the result of a general tracking algorithm (b).

displayed. Neutrino interactions identified in the emulsion can be examined near the primary vertex down to micrometer level. A typical neutrino event in a single emulsion layer perpendicular to the neutrino beam is shown in Figure 4.2a. The clearly visible black tracks are mainly heavily ionizing fragments from nuclear breakup in the interaction emitted at large scattering angles. The particles resulting directly from the partonic neutrino interaction are usually minimum ionizing, and produced in the forward direction. Since Figure 4.2a is only a two dimensional thin emulsion slice, particles going into the forward direction manifest themselves in this projection only in single spots; thus they are not recognizable as tracks in this figure. To visualize those tracks, a series of parallel emulsion layers allowing recording in a third dimension is needed. An outcome of such a three dimensional reconstruction (*general tracking*) is displayed in Figure 4.2b.

4.1.2 Correcting the data

To locate a neutrino interaction and - in particular - a charmed particle decay in the emulsion, several analysis steps have to be made. If a neutrino has interacted in the emulsion the event is expected to also have triggered the data acquisition, and to have been reconstructed from the electronic detector data.

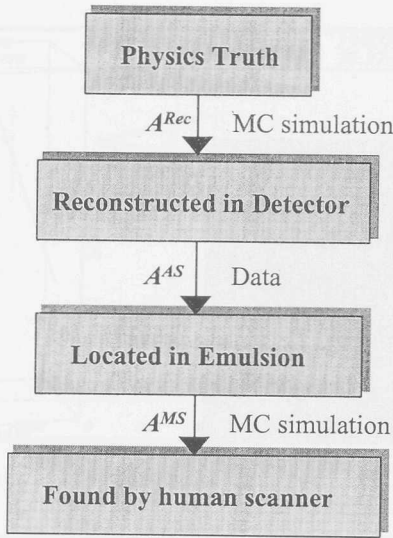


Figure 4.3: Flow diagram visualizing the gradual steps in the analysis of a complete physics sample of charm events.

The reconstructed particle trajectories followed backwards *predict* tracks in the emulsion. The automatic microscopes have to *locate* and trace these tracks further backwards in the emulsion, from plate to plate until a primary vertex is found. Only then the emulsion plate and coordinates of the vertex position are known so that an operator (scanner) can examine such an event in detail.

In every step of the above procedure losses and smearing occur. These depend often on instrumental (and indirectly on kinematical) characteristics. They have to be taken into account, before an original 'physics true' distribution can be quantitatively associated with the corresponding measured distribution. Conversely, we want to design a procedure that - given a measured distribution - allows to reconstruct as closely as possible the corresponding 'physics true' distribution. For this purpose, we first describe in the following the flow diagram from a simulated 'physics truth' towards the final distribution of measured events (Figure 4.3) in more detail.

- **Detector reconstruction acceptance A^{Rec}**

Neutrino events are triggered in the detector and reconstructed with a certain kinematic acceptance probability (short: acceptance) and (in)efficiency (e.g. due to dead time, misalignment, etc.). Similarly, it has to be taken

into account that also in the analysis, e.g. by selecting explicitly a kinematic region, the acceptance is affected. The trigger, reconstruction and explicit kinematic selection together are taken care of in $A^{Rec}(k)$, where k stands for all kinematic variables. It is evaluated by using a MC simulation. Applying our current kinematic selections e.g. for dimuon charm events, A^{Rec} amounts to typically 30%, when integrated over the kinematic variables.

- **Automatic scanning efficiency A^{AS}**

Once a measured event from the electronic detector has been reconstructed, the track exit points on the emulsion stack are predicted. An automatic microscope scanning system locates the predicted tracks, and follows them upstream through the emulsion plates until the primary vertex is found. Tracks and vertices can get lost due to wrong or inaccurate track predictions, as well as due to inefficiencies of the emulsion and/or of the scanning system.

The vertex location efficiency of the automatic scanning process ($A^{AS}(k)$) is evaluated from the analysis of a data sample composed of 2μ events generated from charmed particle decays and pions decaying in flight showing an identical signature in the electronic detector.

In this sample 763 2μ events have been located in the emulsion with respect to an original sample of 2256 preselected 2μ events in the detector. The scanning efficiency A^{AS} integrated over the kinematic dependence is therefore 34%.

Unfortunately, the large number of 1μ events scanned for the oscillation search could not be used for determining A^{AS} due to a 30 GeV upper momentum cut that was applied on the 1μ predictions. Such a cut is unacceptable for our work.

- **Manual scanning efficiency A^{MS}**

In the search for charm events, the located 2μ events are examined manually for decay topologies. Here, for a given event topology the optical system and the human eye introduce an additional acceptance limitation. This function ($A^{MS}(k)$) has been estimated by a MC simulation and verified by a cross check with the charm events found in the data. Taking into account the limited focal depth of the microscopes and the grain density inside the emulsion, a shortest visible flightlength of 10 μm is expected

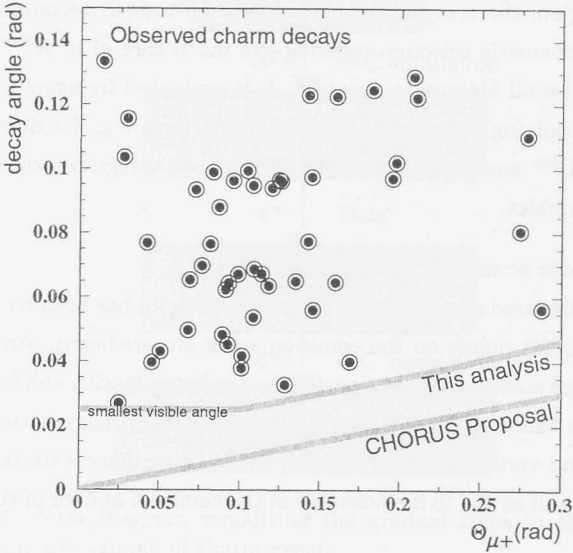


Figure 4.4: Measured decay angle versus track angle (see text).

and assumed in the estimate.

Furthermore, in principle it is expected that inside the emulsion, the smallest visible decay angle increases with the track angle (polar angle with respect to the X-axis). This effect occurs because of the particular emulsion plate orientation with respect to the microscope optics.

It has been found that the (presumed) smallest visible decay angle as a function of the track angle depicted in Figure 4.4 is in good agreement with the observed decays and with our MC studies. The flat behaviour in the range $0 < \theta < 100$ mrad follows from the limited accuracy of the manually measured angles (see Figure 3.14). The linear trend towards zero as described in the CHORUS proposal (see Figure 4.4) may thus be too optimistic for our present data set.

For part of the data, additional selection criteria have been applied in order to decrease the manual scanning load. For 1996-1997 data, candidate events have only been scanned manually, if a) the μ^+ and the μ^- stop in different emulsion plates, or b) μ^+ and μ^- stop in the same plate but have a minimum distance of more than $5 \mu\text{m}$. These criteria have been included

in the MC simulation and A^{MS} integrated over kinematics is estimated to be typically 82%.

In the following sections distributions of various kinematic variables are studied. The observed distributions can be corrected for the kinematic acceptances, cuts and (deduced or estimated) inefficiencies to obtain the corresponding 'true' distributions

$$N_{true}(k_j) = \frac{N_{obs}(k_j)}{A(k_j)}, \quad (4.1)$$

where $N_{obs}(k_j)$ is the observed distribution and $A(k_j)$ the acceptance, both as a function of the kinematic variable k_j and integrated over all other kinematic variables. For charm events, the acceptance function is

$$A(k_j) = A^{Rec}(k_j) A^{AS}(k_j) A^{MS}(k_j). \quad (4.2)$$

In the determination of the charm production cross section described in section 4.2.3 we normalize with respect to the cross section for the CC event sample. However, this CC event sample and the charm sample cannot be compared on the 'emulsion level' without introducing additional biases, because of the unfortunate upper muon momentum cut in the CC sample. Therefore, the corresponding 'true' distributions of CC events observed and reconstructed in the detector are used for the normalization. The 'true' CC data distributions are obtained from the observed distributions according to Equation 4.1 with the acceptance function

$$A(k_j) = A^{Rec}(k_j). \quad (4.3)$$

In summary, the corrections are evaluated by MC simulations and - where possible - by data, taking into account all relevant hardware and software aspects. To get confidence in this procedure, in the following section the physics input coming from CC event generators is compared—as a consistency check—with the deduced 'true' experimental distributions.

4.1.3 Event generation and detector response

For the various topics studied in this thesis, different MC generators have been used. For simulating deep inelastic neutrino interactions, the standard CHORUS event generator JETTA [73] has been employed. It is based on the LEPTO [74] package to simulate ν_μ and ν_τ CC interactions, and JETSET [32]

for hadronization and decays. The structure functions are parameterized according to GRV94LO [75]. In the JETTA generator heavy quark effects are not implemented (see slow rescaling model Equation 2.8).

For extracting physics parameters of charmed hadron production, a new fast and flexible simulation has been developed, based on the event generator MICKEY used for the structure function analysis in the CHORUS calorimeter [44]. This simulation uses also the GRV94LO structure function set and includes heavy quark effects according to the slow rescaling model. The Peterson model (see Equation 2.13) is implemented for the charm fragmentation and particle decays are realized with the JETSET package. For the search of diffractively produced charmed mesons, a new event generator (ASTRA) has been written. The output of the generators has been interfaced to the GEANT [76] based CHORUS detector simulation EFICASS including all details of the detector and providing the appropriate detector response for the MC-generated events.

In the following, some CC distributions obtained with the deep inelastic MC generators are compared with the 'true' data obtained with the correction procedure described in the previous subsection. A kinematic region that is dominated by deep inelastic production is selected. The selection criteria for the data versus MC comparison are $\nu > 2.3 \text{ GeV}$, $Q^2 > 5 \text{ GeV}^2$ and $W^2 > 2 \text{ GeV}^2$.

In Figure 4.5 the one-dimensional projections for the neutrino energy E_ν (a), the momentum of the negatively charged muon p_{μ^-} (b), the Bjorken x (c), the inelasticity y (d), the square of the transferred four-momentum Q^2 (e) and the square of the invariant mass of the hadronic final state W^2 are displayed. The data (1994 - 1995) have been corrected according to Equation 4.1 for instrumental acceptances and inefficiencies and they are compared with the JETTA MC (squares) and MICKEY MC (triangles) simulations. The data and MC distributions are normalized to the same number of entries.

For the E_ν (Figure 4.5a) distribution, data and MC clearly reproduce the shoulder of high energy ($>70 \text{ GeV}$) neutrinos that originates mainly from the kaon contribution in the CERN primary meson beam. The two MC simulations agree with each other, however they deviate from the data points in the low part of the spectrum $120 < E_\nu < 160 \text{ GeV}$. This deviation can be understood in terms of a not fully realistic estimate of horn and reflector current in the neutrino beam simulation [44], of which an output sample serves as input to our physics MC event generation. The deviation which is minor in terms of the integrated

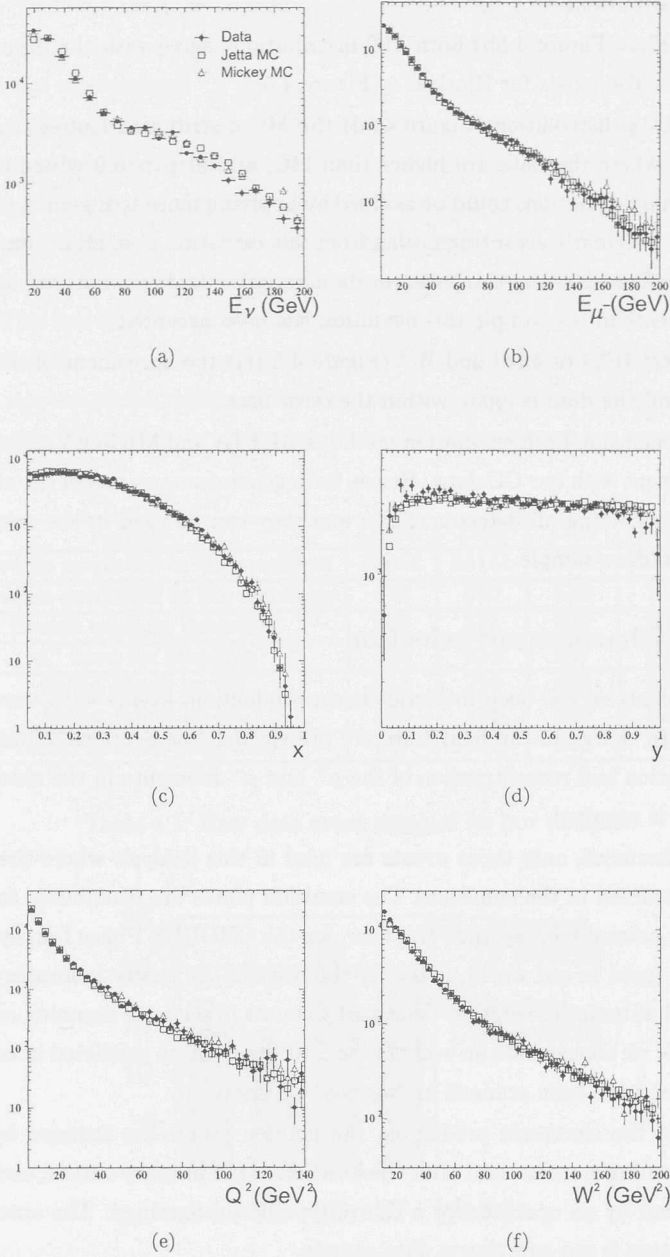


Figure 4.5: Data and MC comparison in 1D projections for various kinematic variables. The black dots represent the - for acceptance - corrected ('true') data, the squares the JETTA MC and the triangles the MICKEY MC ((a) E_ν , (b) E_{μ^-} , (c) x , (d) y , (e) Q^2 , (f) W^2).

beam, anyhow largely cancels in the ratio of charm event distributions and CC event distributions.

For E_{μ^-} (Figure 4.5b) both MC distributions agree with the data. Good agreement also exists for Bjorken x (Figure 4.5c).

In the y -distribution (Figure 4.5d) the MC distributions agree, except at $y < 0.25$ where the data are higher than MC, and at $y > 0.9$ where they are lower. These deviations could be avoided by applying more stringent cuts. However, the systematic error originating from this deviation is small in comparison to the statistical error of the charm data sample. In favour of keeping more charm events in the sample this deviation has been accepted.

For Q^2 (Figure 4.5e) and W^2 (Figure 4.5 (f)) the agreement of both generators and the data is again within the error bars.

In conclusion both simulation methods, JETTA and MICKEY, are in overall agreement with our CC data. Hence, both generators can model the observed CC data including all detector effects and they can be used in the analysis of the charm data sample.

4.1.4 Charm event selection

For our study of CC deep inelastic charm production, events with two muons of opposite charge in the final state are preselected (see Sections 2.2 and 2.4). Identification and reconstruction of the μ^+ and μ^- momenta in the muon spectrometer is required.

Furthermore, only those events are used in this analysis where the vertex is reconstructed in the emulsion. The emulsion plates are distributed for scanning over several laboratories. However, for the CHORUS Phase I analysis and scanning (used in our work), it is only the Nagoya University laboratory - who pioneered automatic scanning - that really counts in terms of scanning capacity. Therefore, we concentrate on events with a vertex position predicted in emulsion plates that have been scanned at Nagoya University.

Using the electronic prediction, the dimuon events are scanned by automatic scanning systems, and after the location of the primary vertex, each event is examined by an operator for a charm-type decay topology. The outcome of this selection is our raw charm data sample.

The CC (1μ) event sample selected for our analysis has one identified muon in the spectrometer with negative charge and a reconstructed vertex in the emulsion. The selected kinematic region is $\nu > 2.3$ GeV, $Q^2 > 5$ GeV² and

$W^2 > 2 \text{ GeV}^2$.

In Table 4.1 the year-by-year event samples with a reconstructed vertex in the emulsion and the events with a vertex located by the automatic scanning system are summarized.

In 1995 and 1997 there are less events with a located vertex in the emulsion target than expected from the number of recorded CC events. The reason is that in 1995 a set of emulsion plates was not usable for scanning because of a damaged surface. The fraction of located vertices in 1997 data is smaller because internal scanning criteria have been changed to decrease the scanning load. This has been taken into account in the analysis.

After the manual scanning, the number of found charm events also reflects in the year-by-year statistics of the automatically scanned and located events as depicted in Figure 4.6. In total a sample of 132 charm decays has been obtained.

Year	1994	1995	1996	1997	all
1μ events predicted in the emulsion	38014	54141	68508	80973	241636
2μ events predicted in the emulsion	378	540	610	724	2252
Events tried for scanning	355	371	583	662	1971
μ^+ tried for scanning	320	311	567	647	1845
Event found on CS	211	216	422	568	1417
Event found on SS	199	198	366	329	1092
Vertex in bulk plate 3-36	137	123	270	233	763

Table 4.1: Raw data event samples for our analysis.

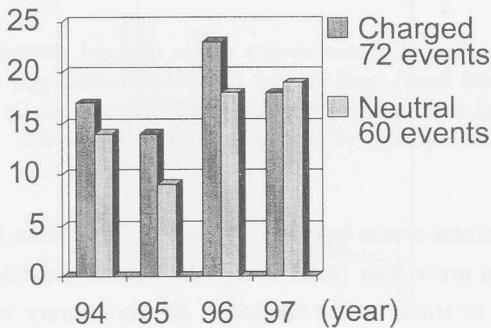


Figure 4.6: Number of charm events found, split into neutral charm and charged charm decays.

4.2 Results

Apart from E531, CHORUS is the only experiment where charmed particles can be directly observed in emulsion, both at the production and at the decay vertex. At the time of this analysis only a limited event sample of muonic charm decays was available (*Phase I* scanning). In view of the *Phase II* event sample, being scanned presently, which includes hadronic decay channels and which is expected to be more than an order of magnitude larger, our analysis can serve as a basis for upcoming studies. In this perspective it is attempted to find an appropriate level of detail in presenting the results.

4.2.1 Charm topologies

In the observed charm decays, contributions from D^0 , D^+ , D_s^+ and Λ_c^+ are expected. In the emulsion, neutral charmed particles can be distinguished from charged charmed particles. However, the particle type (D^+ , D_s^+ or Λ_c^+) cannot be identified on a single event basis.¹ The type of information that can be

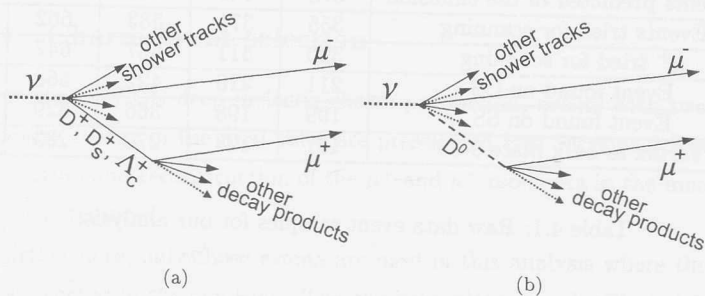


Figure 4.7: Topology of charm events where charged particles are visible in the emulsion (solid lines), and neutral particles (dashed and dotted lines) are invisible. Neutral charmed hadrons (dashed line) can usually be identified by the kinematics and topology of the visible parts of the event.

extracted from charm events in emulsion can be judged from Figure 4.7. Only charged particles are visible (solid lines), the neutral particles (dotted lines) can not be seen as tracks in the emulsion. At the primary vertex and at the secondary decay vertex, the number of charged particles can be counted. Furthermore flight lengths and angles of the charmed particles can be measured.

¹It might be possible in the Phase II analysis to reconstruct the invariant mass of the charmed particles with hadronic decays.

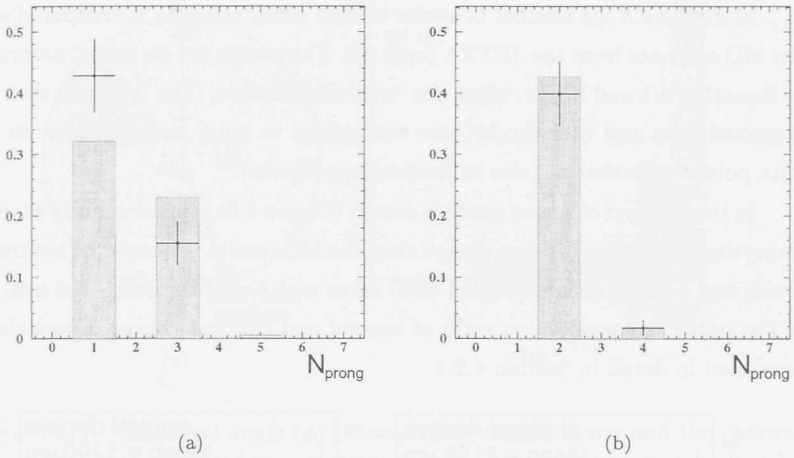


Figure 4.8: Corrected ('true') number of charged decay products N_{prong} for charged charm (a) and neutral charm data (b). The integral is normalized to unity. The data (crosses) are compared with MC (histogram).

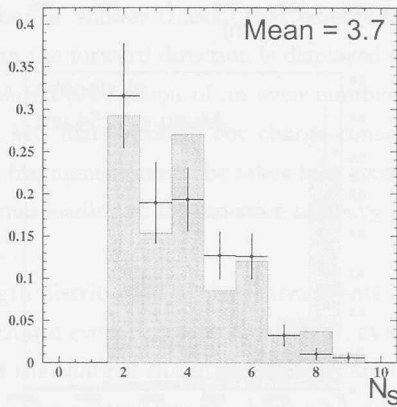


Figure 4.9: Corrected ('true') distribution of the charged track multiplicity N_s at the primary vertex for charm data (crosses) and MC (histogram).

Due to charge conservation, the charged charmed particles decay into an odd number of charged daughter particles (μ^+ included), whereas a neutral charmed particle decay involves two or four charged daughter particles.

In Figure 4.8 the number of events in each decay category is compared with the MC estimate from the JETTA program. The events are corrected according to Equation 4.1 and hence reflect the 'true' distribution. The integrals over the corrected data and over the MC are normalized to unity and the error on the data points is statistical (also in forthcoming figures).

In the charged charmed particle decays (Figure 4.8a) we see slightly more 1-prong decays and less 3-prong decays than the MC results, whereas the neutral 2-prong and 4-prong decays (Figure 4.8b) agree with the MC values. The analysis of the particular production ratio of neutral and charged charmed particles is presented in detail in Section 4.2.4.

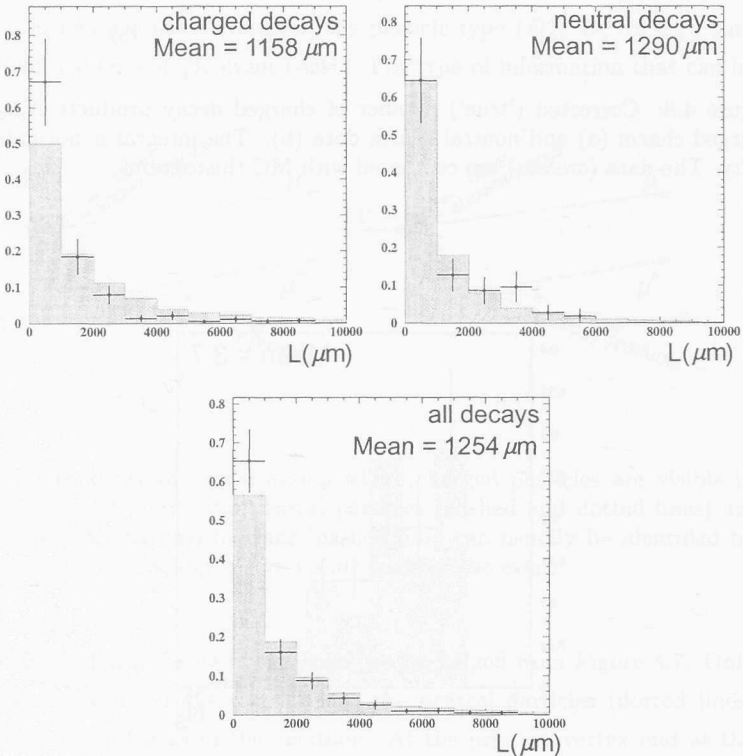


Figure 4.10: Corrected ('true') flight length (L) distribution for data (crosses) and MC (histogram).

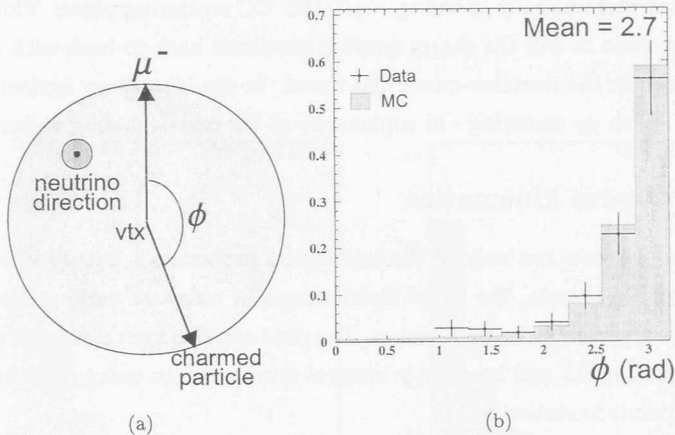


Figure 4.11: Azimuthal angle (ϕ) between the primary muon and the charmed particle trajectory viewed in projection onto the transverse plane (a); distribution as a function of ϕ (b) for corrected ('true') data (crosses) compared with MC (histogram).

An interesting observation here is that the JETTA MC modeling of the fragmentation and jet development at a primary neutrino vertex is rather well described by the string fragmentation model. The observed multiplicity of charged particles N_s (number of 'shower tracks') that emerge from the primary charm production vertex in the forward direction is displayed in Figure 4.9. The overall shape with a biased production of an even number of charged particles is reproduced in the MC distribution. For charge conservation at the primary vertex, the nuclear fragments have to be taken into account. However, the complex nuclear dynamics leading to the emission of heavy nuclear fragments is not modeled in the MC.

The flight length distribution of the charm events is shown in Figure 4.10. While the neutral charm events agree well with MC, at short flight lengths there is a slight excess of the charged charm events compared with the MC estimate. We studied whether this excess hints at a higher Λ_c^+ contribution than modeled in the MC simulation. However, within the limited statistics of the sample this could not be found in other kinematic projections.

The azimuthal angle at the primary vertex between the primary μ^- trajectory and the charmed hadron trajectory, projected on the plane transverse to

the neutrino beam direction, is displayed in Figure 4.11. The charmed particle is produced preferentially in the $\nu_\mu - \mu^-$ DIS CC scattering plane. This is expected, because in DIS the charm quark is produced back-to-back with respect to the muon in the neutrino-quark CM frame. In the laboratory system this is reflected - with p_T smearing - in coplanarity of the corresponding momenta.

4.2.2 Charm kinematics

To get an overview not only of the topological properties - but also the kinematics - of the events, the 'true' distributions in terms of various kinematic variables are presented in this section. The data are also here corrected according to Equation 4.1 and have their integral normalized to unity. The error on the data points is statistical.

Figure 4.12 shows the 'true' distributions for E_{μ^-} , E_{μ^+} , E_ν and Q^2 , whereas Figure 4.13 shows them for W^2 , Bjorken- x , y and z_μ .

The overall agreement with the MC distributions is good. In W^2 there is perhaps an excess in the data at low W^2 . The y -distribution shows for the data large bin-by-bin statistical fluctuations.

The secondary muon is identified by its positive charge. As expected, it is usually less energetic than the primary (negatively charged) muon from the CC interaction. The average energy of the interacting neutrinos producing a charmed particle ($\langle E_\nu^{\text{charm}} \rangle = 56.4$ GeV) is higher than in a CC interaction ($\langle E_\nu^{\text{CC}} \rangle = 49.3$ GeV), also as expected.

In the following subsection we use the shape of distributions to extract certain parameters for modeling the production process of charmed particles by neutrinos. In particular, we use the energy distribution to extract the charm quark mass, the x -distribution to get information on the strange sea component, and the z_μ -distribution to derive a fragmentation parameter.

4.2.3 Charm cross section

The charmed particle cross section at different neutrino energies has been a controversial topic for many years. Charm quark mass effects are expected to manifest themselves as a threshold effect in the energy distribution. The big advantage of the CHORUS experiment is that the charmed particles can be directly observed and tagged, whereas in most of the previous experiments it was only possible to observe the final state particles. It was neither possible to see the primary vertex nor the charmed particle decay giving substantial

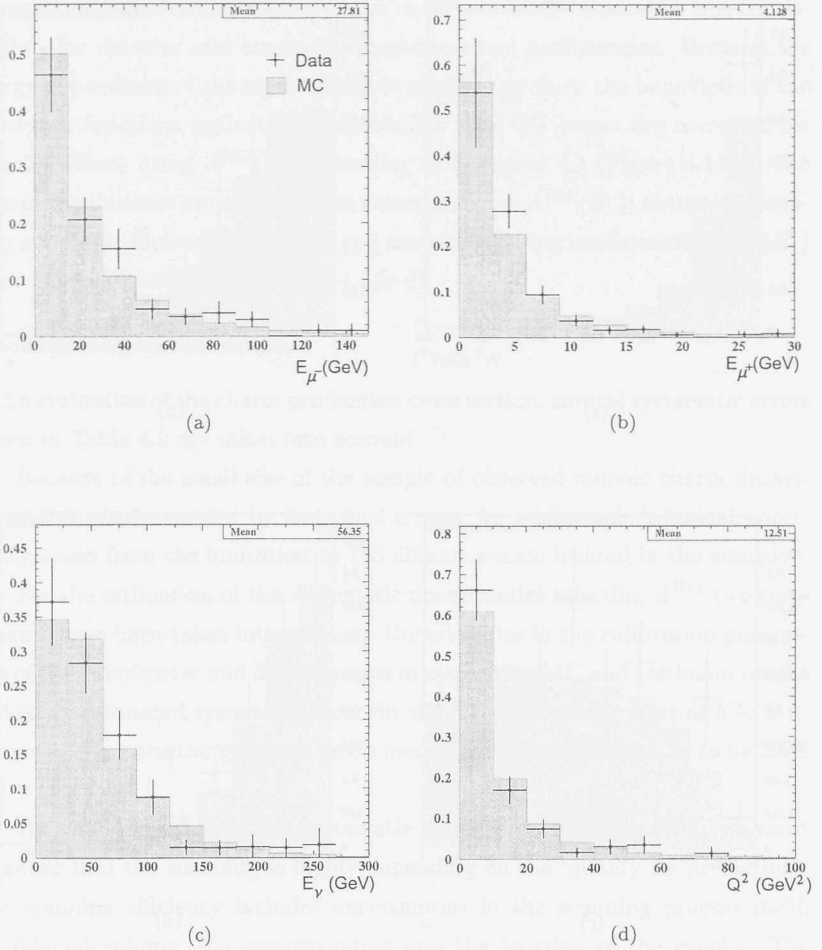


Figure 4.12: Corrected ('true') event distributions for kinematic variables (a) $E_{\mu-}$, (b) $E_{\mu+}$, (c) E_{ν} and (d) Q^2 . The data (crosses) are compared with MC (histogram).

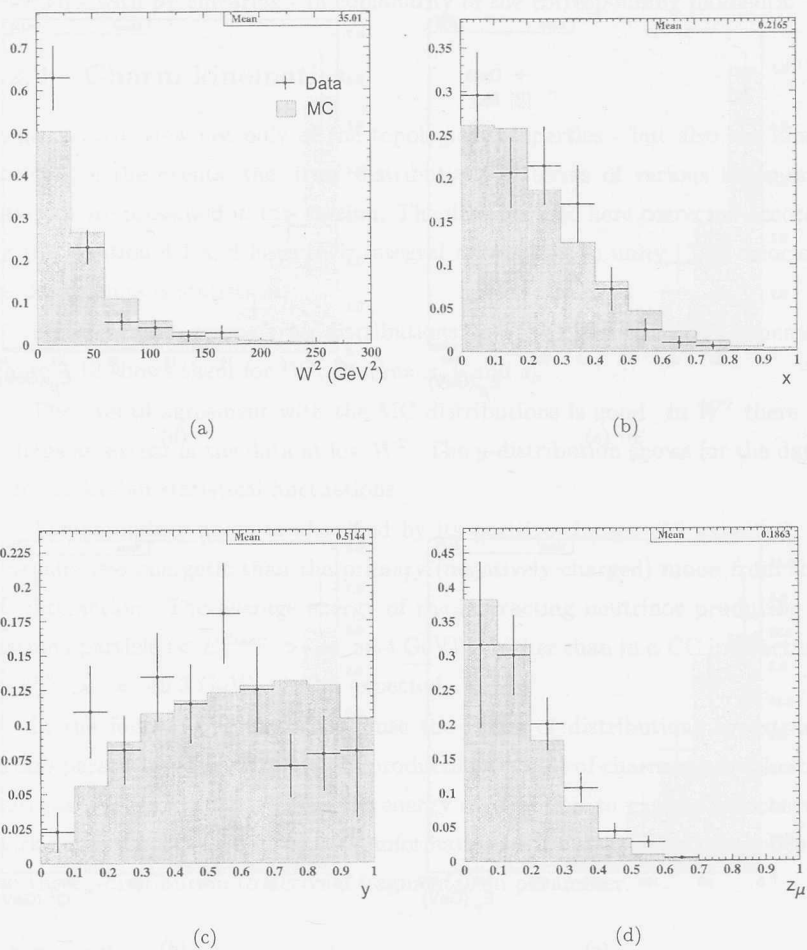


Figure 4.13: Corrected ('true') event distributions for kinematic variables (a) W^2 , (b) x , (c) y and (d) z_μ . The data (crosses) are compared with MC (histogram).

uncertainties. Furthermore, in CHORUS the charm production cross section can be separated into charged and neutral contributions. Until now only in E531 this distinction could be made.

The charm cross section is here calculated per CC interaction. To obtain the 'true' distributions, both the full CC distributions and the kinematically corresponding charm distributions have to be corrected - separately but consistently - for detector and emulsion acceptances and inefficiencies. Because the energy dependence of the cross section is studied, we show the behaviour of the correction functions against the variable E_ν . The CC events are corrected for detector effects using $A^{Rec}(E_\nu)$ according to Equation 4.1 (Figure 4.14a). The charm distributions are corrected for detector effects $A^{Rec}(E_\nu)$, automatic scanning system inefficiencies $A^{AS}(E_\nu)$ and manual scanning inefficiencies $A^{MS}(E_\nu)$ according to Equation 4.1 (Figure 4.14b-d).

Discussion of uncertainties

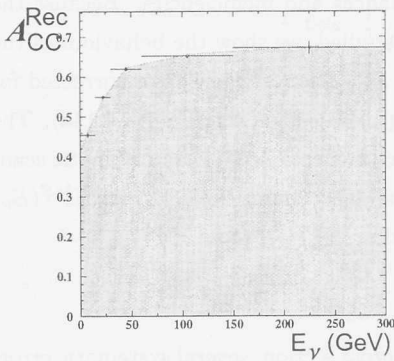
In the evaluation of the charm production cross section, several systematic errors shown in Table 4.2 are taken into account.

Because of the small size of the sample of observed muonic charm decays, the analysis is dominated by statistical errors. An additional statistical uncertainty arises from the limitation to 763 dimuon events located in the emulsion.

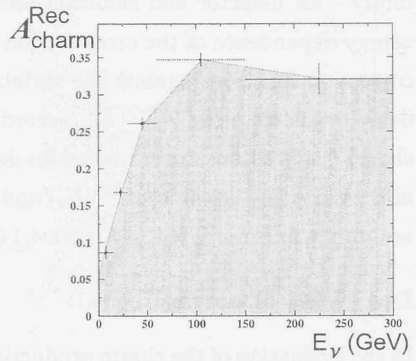
For the estimation of the systematic uncertainties affecting A^{Rec} two components have been taken into account. Uncertainties in the calibration parameters of the calorimeter and discrepancies in comparing MC and testbeam results lead to an estimated systematic error for the hadronic energy scale of 5%. Furthermore, the uncertainty on the muon momentum scale is estimated to be 2.5% [77].

For the estimation of the systematic uncertainty affecting A^{AS} , we must be aware that the scanning is highly depending on the 'quality' of predictions. The scanning efficiency includes uncertainties in the scanning process itself, the fiducial volume, the reconstruction and the location of the events. The systematic error has been evaluated from results of different scanning strategies. On average, the systematic uncertainty in A^{AS} is estimated (conservatively) to be 15%. It is by far the largest uncertainty because it enters directly into the charm cross section.² It has been tried [78] to simulate the entire scanning

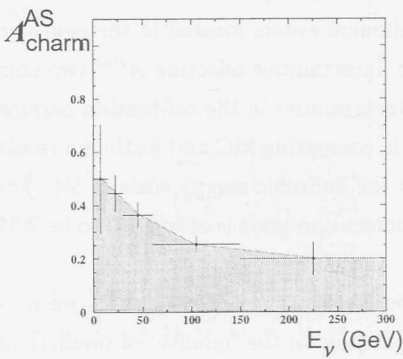
²This is one of the reasons, why for the CHORUS Phase II scanning the 1μ events are scanned without cut on the muon momentum. This results in a CC sample for the automatic scanning correction that is about a factor 20 larger than the currently used sample. Hence, this contribution to the systematic uncertainty will be reduced drastically in the future by



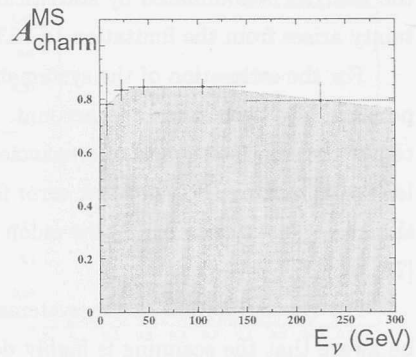
(a)



(b)



(c)



(d)

Figure 4.14: Distributions of the various correction factors as a function of E_{ν} for the CC and charm samples.

Source of systematic uncertainty	$\Delta \frac{\sigma(\text{charm})}{\sigma(\text{CC})}$
Hadronic energy scale (5%)	0.14
Muon momentum scale (2.5%)	0.05
Reconstruction and Scanning	0.69

Table 4.2: Systematic uncertainties.

system and procedure, however, no consistent agreement with the data could be reached in sufficient detail.

Charm cross section

After having corrected the data leading to the corresponding 'true' distributions, it is possible to plot the charm production (with muonic decay) per CC interaction versus neutrino energy (Figure 4.15a). The overlaid histogram shows the expectation from MICKEY MC calculation using a charm quark mass $m_c = 1.3$ GeV and muonic branching ratios (see Equations 2.17 and 2.18) according to Table 2.2. The charm yield can be split into a charged (Figure 4.15b) and a neutral contribution (Figure 4.15c).

There is an overall agreement of the measured charm yield and the MC simulation. In the charged charm production the data overshoot the expectations in the second bin, whereas there are no entries in the first bin. This can be understood in terms of the rather steep rise in A^{Rec} below 50 GeV (see Figure 4.14b). Therefore we can assume that the observed excess is of statistical nature.

Over the full energy range, the measured overall charm yield per CC interaction results in

$$\frac{\sigma_{\text{charm}} \cdot B_{c \rightarrow \mu}}{\sigma_{\text{CC}}} = (4.6 \pm 0.4 \pm 0.7) \times 10^{-3}, \quad (4.4)$$

$$\frac{\sigma_{\text{charged charm}} \cdot B_{\Sigma h^{ch} \rightarrow \mu}}{\sigma_{\text{CC}}} = (2.7 \pm 0.3 \pm 0.4) \times 10^{-3}, \quad (4.5)$$

$$\frac{\sigma_{D^0} \cdot B_{D^0 \rightarrow \mu}}{\sigma_{\text{CC}}} = (1.9 \pm 0.3 \pm 0.3) \times 10^{-3}, \quad (4.6)$$

where the first error is statistical and the second systematic.

using Phase II data.

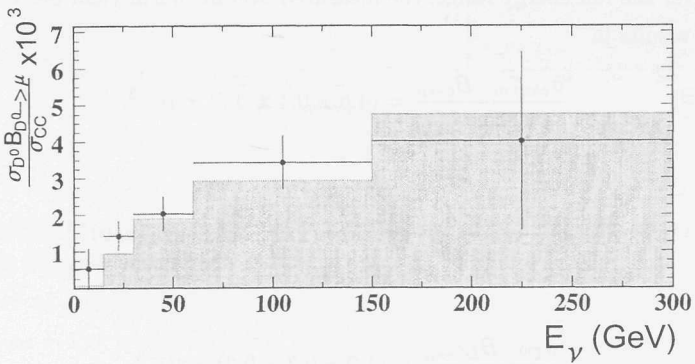
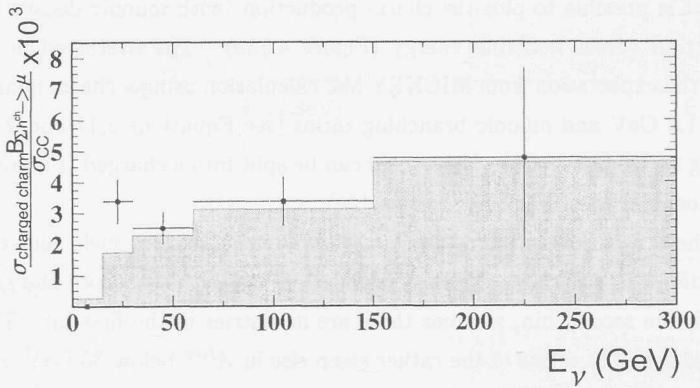
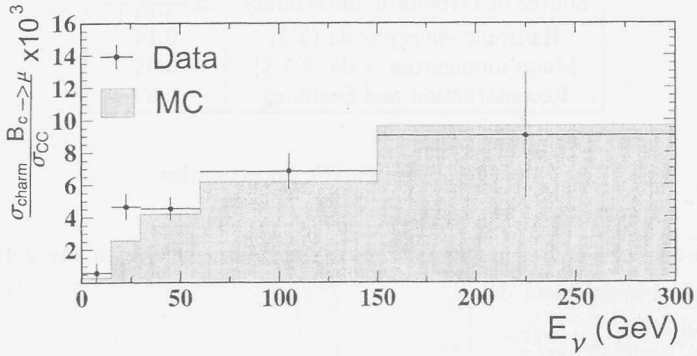


Figure 4.15: Corrected ('true') charmed hadron production with (semi-)muonic decay per CC interaction for all charm (a), charged charm (b) and neutral charm (c) as a function of neutrino energy.

Comparison with results from other experiments

In Figure 4.16 the results of the cross section ratio for charmed hadron production per CC with a muonic decay as a function of neutrino energy is compared with results from previous experiments. Within the errors there is good agreement with NOMAD, CCFR and the emulsion experiment E531. The CDHS data tend to be slightly lower than those of the other experiments, including our results, particularly at low energy.

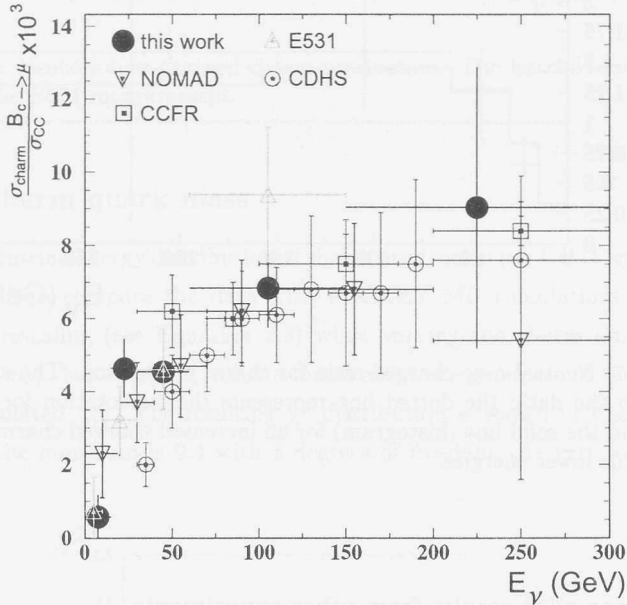


Figure 4.16: Corrected ('true') charm/CC cross section ratio (with muonic decay) from the present work compared with results of previous experiments.

4.2.4 Neutral charm versus charged charm

Having measured the charm/CC cross section ratio including the muonic branching ratio separately for charged and for neutral charm production, it is possible to examine the dependence of the neutral-charged ratio on the neutrino energy.

Assuming the muonic branching ratios $B_{D^0 \rightarrow \mu} = 6.6\%$ and $B_{\Sigma^+ h^+ \rightarrow \mu} = 10.0\%$ (see Section 2.4), we can calculate the energy dependent ratio of neutral and charged charm production, and the result is shown in Figure 4.17. Also in this figure, the assumptions of a constant ratio (dotted line)

and a charged contribution increasing towards low energies [17] (solid line) are shown.

There is a slight tendency in the data that at low energies the charged particle component is higher than at high energies. If confirmed with higher statistics, this can support the hypothesis of a higher quasi-elastic Λ_c contribution [17] at low energies, although no explicit excess of events with such characteristics could be identified in other kinematic projections.

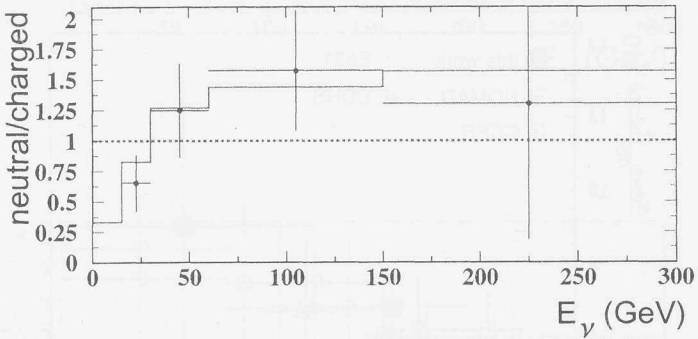


Figure 4.17: Neutral-over-charged ratio for charm production. The crosses correspond to the data; the dotted line represents the expectation for a flat behaviour and the solid line (histogram) for an increased charged charm contribution towards lower energies.

Comparison with results from other experiments

While for cross section measurements of overall neutrino-induced charm production various experiments contribute, before CHORUS experimental data for distinctly identified neutral and charged charm production are limited to the E531 emulsion experiment. Since in this experiment a full kinematic reconstruction of the hadronic charm decays could be performed, it was possible to identify the type of charmed particle on a single event basis. A reanalysis [17] gave production fractions for different charm types as shown in Figure 2.2. The data of Figure 2.2 are converted into the neutral-over-charged charm production ratio and overlayed with the CHORUS experimental results in Figure 4.18.

Within the error bars, the CHORUS data points agree with the E531 measurement, which is consistent with an enhanced fraction of Λ_c events at low energy.

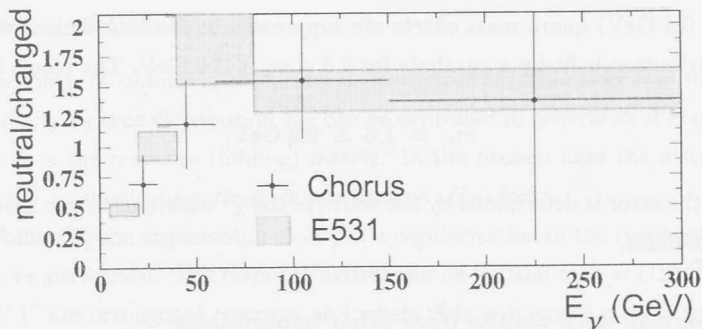


Figure 4.18: Neutral-over-charged charm production. The hatched area corresponds to the E531 measurement.

4.2.5 Charm quark mass

Using the neutrino energy distribution of charm production per CC (Figure 4.15a), it is possible to compare the data with MICKEY MC calculations that include slow rescaling (see Equation 2.8) while varying the charm quark mass parameter (m_c). For every m_c value a measure for the goodness of the fit (χ^2) can be calculated [5]. The resulting χ^2 distribution is shown in Figure 4.19. The χ^2 at the minimum is 9.4 with 5 degrees of freedom. At very low values

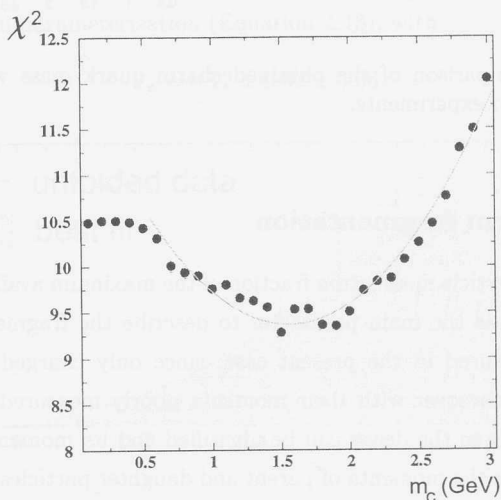


Figure 4.19: χ^2 distribution as a function of the charm quark mass (see text).

($m_c \leq 0.5$ GeV) quark mass effects are suppressed in the MC. This is why the χ^2 distribution is fit by a parabola for $0.6 \leq m_c \leq 3.0$ GeV. The result is

$$m_c = 1.6 \pm 0.8 \text{ GeV}, \quad (4.7)$$

where the error is determined by the width of the χ^2 distribution one unit above the minimum.

Comparison with results from other experiments

In Table 4.3 the above deduced mass parameter is compared with other measurements. The central value of our measurement is larger than the central values obtained by CCFR and NOMAD and less than those from CHARM II and the CHORUS calorimeter analysis. Within the error bars there is a good overall agreement with the other measurements.

Experiment	m_c (GeV)	Ref
CHARM II	1.8 ± 0.4	[79]
CCFR	1.3 ± 0.2	[80]
NOMAD	1.3 ± 0.4	[81]
CHORUS calo	2.1 ± 0.9	[82]
this analysis	1.6 ± 0.8	

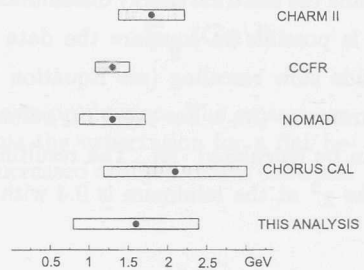


Table 4.3: Comparison of the obtained charm quark mass with values from various neutrino experiments.

4.2.6 Charm fragmentation

The charmed particle momentum fraction of the maximum available momentum (z), often used as the main parameter to describe the fragmentation process, cannot be measured in the present case, since only charged decay products are observed (moreover with their momenta poorly measured). However, the positive muon from the decay can be identified and its momentum can be well measured. Since the momenta of parent and daughter particles in the decay are correlated, the measured value z_μ (see Equation 2.15) can be used to obtain the charmed particle z value. In the following an unfolding procedure is introduced and then applied to our data.

Unfolding procedure

The problem of unfolding a measured (histogram) distribution H_M to obtain the underlying true distribution H_T can be expressed in general as $A H_M = H_T$, where A is the response (folding) matrix. In the present case the distribution (H_M) for z_μ should be converted into the one (H_T) for z .

Following the argumentation in [83] a regularization of the response matrix has to be performed. The response matrix can be written as $A = USV^T$, where U and V are orthogonal matrices and where S is a diagonal matrix with non-negative values. After this decomposition, the solution becomes $H_M = VS^{-1}U^T H_T$. The regularization of the solution is obtained by adding a term of the form $\sqrt{\tau}CH_M$ to the equation, where the matrix C is chosen such as to minimize the second derivative of the unfolded distribution and where the parameter τ is the regularization parameter. A complete description of this method can be found in [83].

Extraction of the fragmentation parameter ϵ_p

The response matrix A , necessary for the unfolding procedure has been extracted from MC simulations. Applying the unfolding method described above on the observed distribution for z_μ (Figure 4.13d) results in the distribution shown in Figure 4.20, which can be fit directly in a standard way by a parameterization for the fragmentation process. The solid curve in Figure 4.20 shows the best fit for the Peterson parameterization (Equation 2.13), with

$$\epsilon_p = 0.12 \pm 0.02 \pm 0.06. \quad (4.8)$$

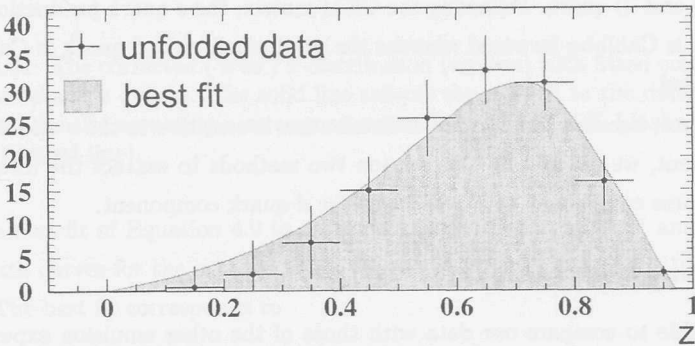


Figure 4.20: Unfolded 'true' z -distribution of charm events with a Peterson fragmentation model fit.

The first error is the statistical error and the second error is attributed to systematic uncertainties in the unfolding procedure estimated by varying the input distributions in the evaluation of the response matrix.

Comparison with results from other experiments

In Table 4.4 the obtained result is compared with results from other neutrino experiments. While the results from CCFR and the CHORUS calorimeter analysis are not compatible with the results of CHARM II and E531, our result agrees with all other measurements of ϵ_P within the error bars.

Experiment	ϵ_P	Ref.
CCFR	0.20 ± 0.04	[80]
CHARM II	0.072 ± 0.017	[84]
E531	0.076 ± 0.014	[85]
CHORUS calo	0.28 ± 0.11	[82]
this analysis	0.12 ± 0.06	

Table 4.4: Comparison of the here obtained Peterson parameter (ϵ_P) with values from other neutrino experiments.

4.2.7 Strange sea

In deep inelastic scattering (DIS), the Bjorken- x value is a measure for the struck quark (longitudinal) momentum, where valence and sea quarks carry on average significantly different fractions of the nucleon momentum. In CC DIS charm production the interaction takes place either on a valence d quark or on a sea (s and d) quark. Following the CKM matrix, the c quark production on a s quark is Cabibbo-favoured whereas the production on a d quark is Cabibbo-suppressed.

Hence, because the Bjorken- x distribution is sensitive to the s and d quark component, we describe in this section two methods to extract the integrated strangeness component with respect to the d quark component.

E531 parameterization

To be able to compare our data with those of the other emulsion experiment E531, we follow their approach [85, 86, 87], where the valence d quark distribution is parameterized as $xd(x) \propto \sqrt{x}(1-x)^\alpha$ and the sea quark distribution as $xs(x) \propto (1-x)^\beta$. Thus the total Bjorken- x quark distribution can be written

as

$$\begin{aligned} \frac{dN}{dx} &\propto N_d V_{cd}^2 \sqrt{x}(1-x)^\alpha + N_s V_{cs}^2 (1-x)^\beta \\ &\propto \sqrt{x}(1-x)^\alpha + f(1-x)^\beta, \end{aligned} \quad (4.9)$$

with N_s and N_d as the fractional d quark and s quark normalizations and V_{cd} , V_{cs} the CKM matrix elements. The variable f summarizes $(N_s/N_d)(V_{cs}^2/V_{cd}^2)$. The exponents are taken as $\alpha = 3.5 \pm 0.5$ and $\beta = 7.0 \pm 1.0$ [85, 86, 87, 88, 89].

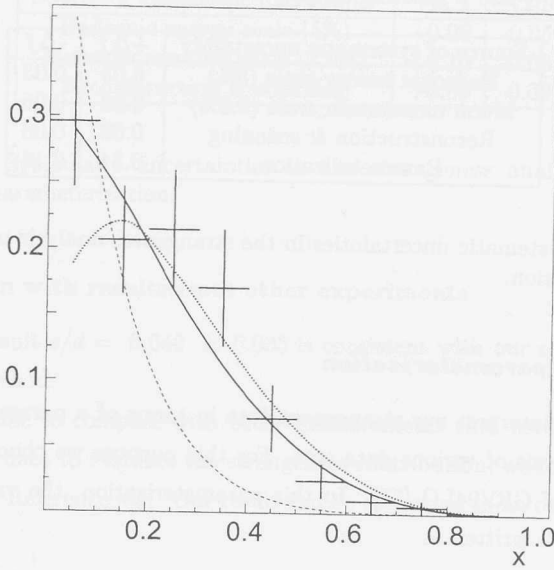


Figure 4.21: The corrected ('true') x -distribution (crosses) with fitted contributions from d and s quarks. The solid line reflects the best fit to the data. Also shown are the fits assuming a strangeness contribution of 100% (dashed line) and 0% (dotted line).

The best fit of Equation 4.9 to our data is shown in Figure 4.21 and compared with curves for the extreme cases where the s quark fraction is 0% and 100%. The best fit corresponds to

$$f = 0.27 \pm 0.15 \begin{matrix} +0.36 \\ -0.19, \end{matrix} \quad (4.10)$$

where the first error is statistical and the second systematic. Using this value

for f the sea quark component results in the integrated strangeness-down ratio

$$\frac{s}{d} = 0.014 \pm 0.007 \begin{matrix} +0.019 \\ -0.010 \end{matrix}. \quad (4.11)$$

In the systematic errors of f and s/d the various contributions as summarized in Table 4.5 are added in quadrature.

Varying the hadronic energy scale by 5% and the muon momentum scale by 2.5% results in systematic uncertainties in A^{Rec} reflected in a variation of the fit result Δf . Systematic uncertainties in the reconstruction and scanning are evaluated by variations in the results for different scanning strategies. The dominant contribution in the systematic error results from the uncertainties in the exponents α and β entering directly in the fit result.

Source of systematic uncertainty	$+\Delta f$	$-\Delta f$
Hadronic energy scale (5%)	0.03	0.03
Muon momentum scale (2.5%)	0.06	0.05
Reconstruction & scanning	0.08	0.08
Parameterization	0.34	0.16

Table 4.5: Systematic uncertainties in the strangeness analysis using the E531 parameterization.

GRV94LO parameterization

We can also interpret our strangeness data in terms of a parameterization for a QCD analysis of various data sets. For this purpose we choose the parameterization of GRV94LO [75]. In this parameterization, the valence d quark distribution is written as

$$xd(x, Q^2) = Nx^a(1 + Ax^b + Bx + Cx^{3/2})(1-x)^D, \quad (4.12)$$

and the strange sea parameterization is written as

$$xs(x, Q^2) = \frac{S^\alpha}{(\ln(1/x))^\alpha} (1 + A\sqrt{x} + Bx)(1-x)^D \cdot e^{(-E + \sqrt{E'S^\beta \ln(1/x)})}, \quad (4.13)$$

where a , b , α , β , N , A , B , C , D , E and E' are determined by a global fit to data, and where S is defined as

$$S = \ln \frac{\ln(Q^2/(0.232 \text{ GeV})^2)}{\ln(\mu_{LO}^2/(0.232 \text{ GeV})^2)}. \quad (4.14)$$

The distributions are evaluated at our $\langle Q^2 \rangle = 12 \text{ GeV}^2$ for $\mu_{LO}^2 = 0.232 \text{ GeV}^2$ [75].

Fitting the GRV94LO parameterization to our data results in

$$f = 0.47 \pm 0.22 \begin{matrix} +0.15 \\ -0.13 \end{matrix}, \quad (4.15)$$

and thus

$$\frac{s}{d} = 0.024 \pm 0.011 \begin{matrix} +0.008 \\ -0.007 \end{matrix}. \quad (4.16)$$

The systematic errors summarized in Table 4.6 are added in quadrature. The systematic errors have been derived in a similar way as for the E531 parameterization, but no uncertainties in GRV94LO parameters are taken into account.

Source of systematic uncertainty	$+\Delta f$	$-\Delta f$
Hadronic energy scale (5%)	+0.06	-0.05
Muon momentum scale (2.5%)	+0.10	-0.08
Reconstruction & scanning	+0.09	-0.09

Table 4.6: Systematic uncertainties in the strangeness analysis using the GRV94LO parameterization.

Comparison with results from other experiments

The E531 result $s/d = 0.042 \pm 0.033$ is consistent with our result, based on the same method.

To be able to compare with other measurements that used neutrino and antineutrino data to evaluate the strangeness contribution, we follow the argumentation in Reference [85]. Our result can be converted to an other parameter value

$$\eta_s = \frac{2s}{u + d}, \quad (4.17)$$

by assuming equal up and down quark content. The result can also be expressed in the parameter

$$\kappa = \frac{2s}{\bar{u} + \bar{d}}, \quad (4.18)$$

by using the total quark/antiquark ratio measured by CCFR $q/\bar{q} = 0.153$ as in reference [90].

In Table 4.7 and Table 4.8 the various experimental results on η_s and κ are listed.

Within the error bars, our result generally agrees only with the E531 experiment that was based on similar assumptions. The central values that we

obtain for the strangeness parameter values are systematically below the other measurements.

Experiment	η_s	Ref
CDHS	0.061 ± 0.005	[79]
CHARM II	0.068 ± 0.014	[84]
CHARM	0.050 ± 0.015	[86]
CCFR	0.064 ± 0.015	[80]
E531	0.042 ± 0.033	[85]
NOMAD	0.071 ± 0.023	[81]
this analysis	0.024 ± 0.014	

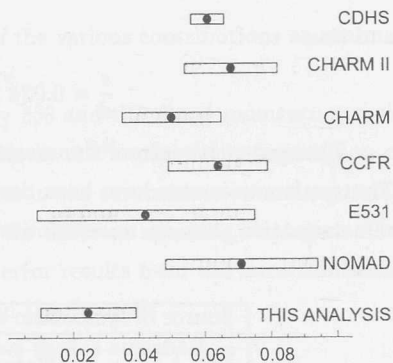


Table 4.7: Comparison of η_s values from different experiments.

Experiment	κ	Ref
CDHS	0.47 ± 0.09	[79]
CHARM II	0.39 ± 0.10	[84]
CHARM	0.39 ± 0.12	[86]
CCFR	0.44 ± 0.11	[80]
E531	0.32 ± 0.25	[85]
NOMAD	0.48 ± 0.19	[81]
CHORUS calo	0.26 ± 0.11	[82]
this analysis	0.17 ± 0.11	

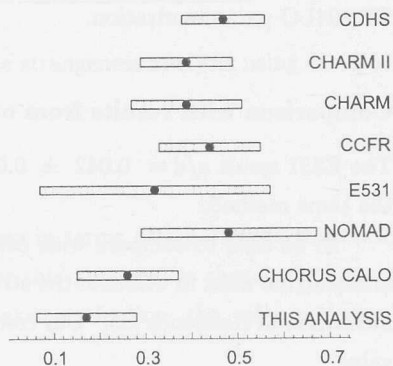


Table 4.8: Comparison of κ values from different experiments.

4.2.8 Weak mixing V_{cd}

Combining the measurements on $B_{c \rightarrow \mu} |V_{cd}|^2$ from CCFR [91] and CDHS [79] gives [17]

$$B_{c \rightarrow \mu} |V_{cd}|^2 = (5.02_{-0.69}^{+0.50}) \times 10^{-3}. \quad (4.19)$$

The average muonic decay branching ratio ($B_{c \rightarrow \mu}$) includes for every producible charmed particle type also the corresponding production fraction (ac-

according to Equation 2.17)

$$B_{c \rightarrow \mu} = P_{D^0} B_{D^0 \rightarrow \mu X} + P_{D^+} B_{D^+ \rightarrow \mu X} + P_{D_s^+} B_{D_s^+ \rightarrow \mu X} + P_{\Lambda_c^+} B_{\Lambda_c^+ \rightarrow \mu X}. \quad (4.20)$$

Our present CHORUS data set does not allow to determine the charged charm composition independently. Only the charged-over-neutral charm ratio is measured. This quantity can be incorporated in Equations 4.19 and 4.20 to extract V_{cd} .

Folding the E531 E_ν dependent charged charm production fractions with the CHORUS neutrino beam spectrum results in contributions of $(42 \pm 10) \% D^+$, $(29 \pm 21) \% D_s^+$ and $(29 \pm 16) \% \Lambda_c^+$ to the charged charmed hadron sample (see Section 2.2).

The total charged-over-neutral charm production ratio ϱ_c as obtained in our analysis is

$$\varrho_c = 0.90 \pm 0.36. \quad (4.21)$$

From this result, the D^0 contribution to the overall sample can be obtained:

$$P_{D^0} = \frac{1}{1 + \varrho_c} = 0.53 \pm 0.11. \quad (4.22)$$

Using the branching ratios $B_{D^0 \rightarrow \mu X} = (6.6 \pm 0.8) \%$ [29], $B_{D^+ \rightarrow \mu X} = (17.2 \pm 1.9) \%$, $B_{D_s^+ \rightarrow \mu X} = (5.0 \pm 5.4) \%$ [30] and $B_{\Lambda_c^+ \rightarrow \mu X} = (4.5 \pm 1.7) \%$ [31] (see Table 2.1) in Equation 4.20, yields a muonic branching ratio of

$$B_{c \rightarrow \mu} = 0.082 \pm 0.015, \quad (4.23)$$

and in Equation 4.19 the CKM-element

$$V_{cd} = 0.247 \pm 0.028. \quad (4.24)$$

Comparison with results from other experiments

Our experimental value on V_{cd} has been evaluated from direct measurements (including the charged charm production fractions from E531), identifying explicitly the production and decay vertex. The direct measurement of V_{cd} from the E531 experiment yields $V_{cd} = 0.232_{-0.019}^{+0.017}$ [17].

Our central value is like the E531 result (possibly due to the common use of the charged charm production fractions) slightly higher than the value $V_{cd} = 0.221 \pm 0.003$ derived from the unitarity requirement of the CKM matrix, but within the error bars all obtained values are in agreement.

Chapter 5

Diffractive charm production

*Thinking is more interesting than knowing, but
less interesting than looking.*
Johan Wolfgang von Goethe

In this chapter, our search for diffractive charm production by neutrinos is described, where the selection criteria and the analysis procedure are completely different from the analysis of deep inelastic charm production. A theoretical description of diffractive charm production is given in Section 2.3. The search resulted in finding one event that fulfills the requirements for diffractive charm production. The reconstruction, analysis and interpretation of the diffractive event are described in detail below.

5.1 Selection of diffractive D_s^* events

To find diffractively produced charmed mesons, the manual scanning load has to be constrained with a strong preselection and a powerful identification scheme. Therefore, the search for diffractive charm production concentrates on diffractive D_s^* production with the decay cascade $D_s^* \rightarrow D_s \rightarrow \tau \rightarrow \mu$ with a clearly recognizable double-kink signature in the emulsion. Such a signature has already been observed in a pion emulsion exposure experiment [92].

To preselect reactions like $\nu_\mu N \rightarrow \mu^- D_s^{*+} (\rightarrow D_s^+ \gamma) N$, where $D_s^+ \rightarrow \tau^+ \nu_\tau$ and $\tau^+ \rightarrow \mu^+ \nu_\mu \bar{\nu}_\tau$, neutrino events with two muons in the detector are selected. Furthermore, to be sensitive to D_s^{*+} decays, only electromagnetic energy in the calorimeter is allowed, and hadronic showers are

vetoed.

The data sample corresponds to data taken in the years 1994, 1996 and 1997. In total 845 events with a reconstructed vertex in the emulsion are pre-selected. From these, 508 events are manually scanned in the emulsion to check in detail for double-kink signatures.

5.2 Background study

As a background for the diffractive production signature, deep inelastic charm production without charged fragments at the primary vertex is examined. Using the JETTA MC including the hadronization of light quarks at the primary vertex it is found - with a charm production ratio per CC of 5% and a relative fraction of D_s^+ mesons of 7% - that $\lesssim 2\%$ of the events produce no other charged particles at the primary vertex. In total we expect therefore a D_s production rate of less than $7 \times 10^{-5}/CC$ from deep inelastic processes.

Possible background scenarios for the decay chain with the emergence of a double-kink signature are:

- A white kink (elastic scattering without visible nuclear recoil) of a D_s^+ or D^+ charmed meson and a subsequent decay into $\mu^+\nu_\mu X^0$. White kinks of heavy mesons have never been observed and for quantitative estimates we rely on pion data [93].
- A D_s^+ or D^+ meson with subsequent decays into $K^+ X^0$ and $K^+ \rightarrow \mu^+\nu_\mu$.

The probabilities for the different decay scenarios to happen and being detected in a CHORUS emulsion stack have been quantitatively studied with a simulation of the beam, the interactions and the detector response. The expected probabilities are summarized in Table 5.1.

It can be concluded that combining production signature and double-kink decay signature thus gives a background-free sample.

5.3 Detector acceptance and reconstruction efficiency

Simulating the diffractive production of a D_s^* meson according to [27] with the entire decay chain (ASTRA), leads to a total detector efficiency for reconstructing this type of events of

$$A^{Rec} = 0.65 \pm 0.07. \quad (5.1)$$

Possible double-kink scenarios	Probability for the signature in a CHORUS emulsion stack
$D_s \rightarrow \tau \rightarrow \mu$	~ 0.96
$D \rightarrow K \rightarrow \mu$	$\sim 8.6 \times 10^{-4}$
$D \rightarrow \text{white kink} \rightarrow \mu$	$\sim 4.3 \times 10^{-3}$
$D_s \rightarrow \text{white kink} \rightarrow \mu$	$\sim 4.3 \times 10^{-3}$
$D_s \rightarrow K \rightarrow \mu$	$\sim 1.9 \times 10^{-4}$

Table 5.1: Possible scenarios to detect a double-kink signature inside a stack of CHORUS emulsion.

The uncertainty on the reconstruction efficiency of 10% is an ad-hoc estimate predominantly accounting for uncertainties in the theoretical description of the event kinematics in the simulation.

Out of the preselected 845 detector events, 508 events have a located vertex thus giving an emulsion location efficiency of

$$A^{AS} = 0.60 \pm 0.02. \quad (5.2)$$

The uncertainty on the scanning efficiency is calculated from the statistical error of the number of events used for the evaluation.

Since there are two decays in the decay chain, the manual scanning efficiency is expected to be high, and has been evaluated by the MC simulation to be

$$A^{MS} = 0.96 \pm 0.03. \quad (5.3)$$

5.4 Reconstruction of a candidate event

Topological reconstruction

In the sample of 508 manually scanned events, one event fulfills all requirements of the diffractive selection criteria of Section 5.1 with the unique decay chain. The detector display of this candidate event (Figure 5.1) shows two identified muons of opposite charge sign. The μ^- and μ^+ have measured momenta of (19.6 ± 3.9) GeV and (1.6 ± 0.1) GeV, respectively.

A visible electromagnetic activity, $E_{em} = (0.27 \pm 0.09)$ GeV, observed in the electromagnetic section of the calorimeter, can be assigned to a secondary interaction vertex in the target region. Since the hits associated to this secondary vertex are strongly scattered, no clear track can be reconstructed in the fiber tracker. The secondary vertex most probably arises from photon conversion.

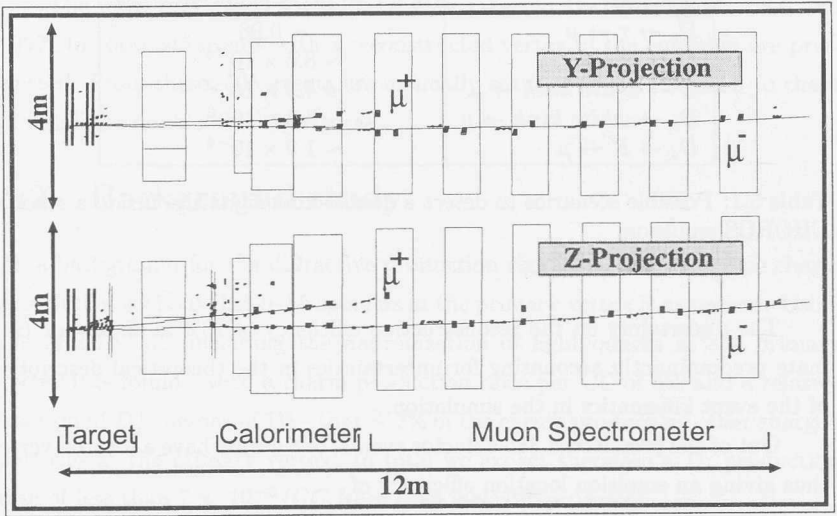


Figure 5.1: Global view of the double kink event in the detector.

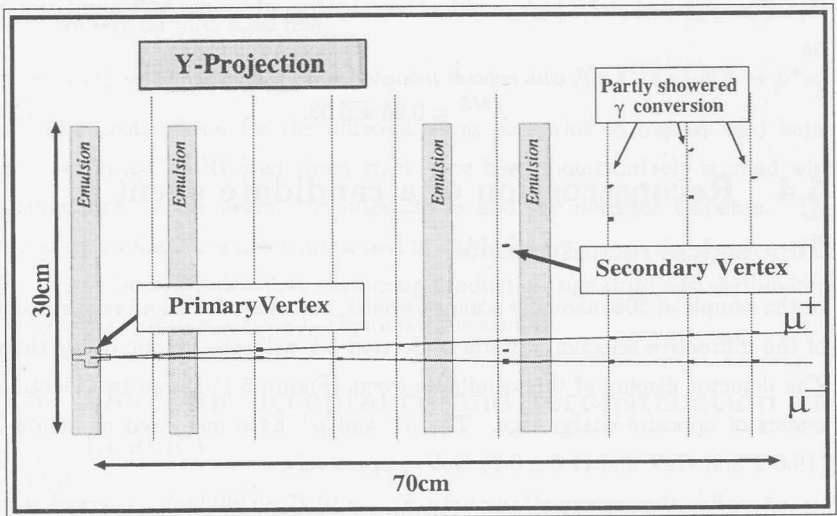


Figure 5.2: Zoom into the target region.

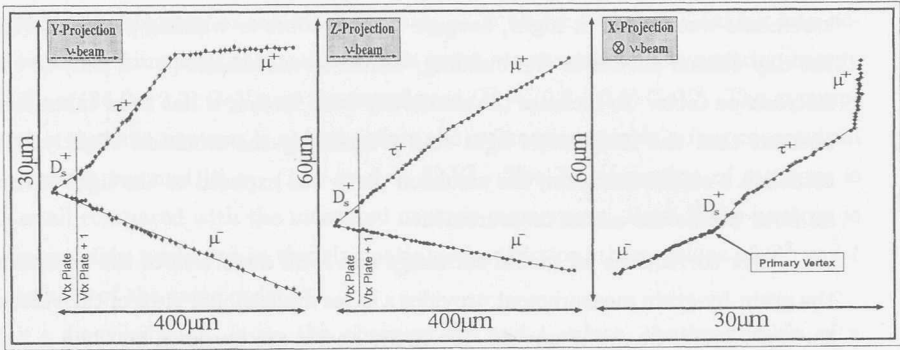


Figure 5.3: The double-kink event with two tracks leaving from a single grain without nuclear break-up at the primary neutrino vertex. The data points represent the measured position of each emulsion grain with its error. Also indicated is the border line between two consecutive emulsion plates.

Furthermore, one isolated hit is detected in a module of the hadronic calorimeter located at a distance of 380 cm downstream of the primary vertex, corresponding to about 1.45 interaction lengths (~ 24.5 radiation lengths). The isolated hit gives a signal of (0.53 ± 0.22) GeV. The signal is isolated and cannot be associated with a charged particle track coming from the primary vertex. In a full detector MC simulation for neutrons generated at the vertex position with momenta of 1 GeV, $\sim 74\%$ of the events show a similar signature in the detector. Together with other aspects of the interpretation of the event it is very probable that the isolated hit is due to the interaction of a neutron coming from the primary vertex.

By tracing back the muon tracks into the emulsion target, a vertex topology is found as shown in Figure 5.3. Two tracks leave from a single grain (size $\sim 1 \mu\text{m}$) without any charged nuclear fragments or recoil.

Because the primary vertex of the event was close to a plate boundary (see Figure 5.3) the topology was difficult to measure. Therefore, the special treatment explained in Section 3.3.3 was applied in order to expand the thickness of the emulsion plates, and thus to increase the accuracy of the grain measurements.

Furthermore, in order to get the highest possible precision on the track angles from the grain measurement, a specific high resolution microscope has been used, with a more stable mechanical support structure and a higher magnification (90x) than needed for standard microscopes. The grain position mea-

measurements were taken at night, because closing doors or walking people during the day caused shocks in the building, visible as movement ($1 - 2 \mu\text{m}$) of the microscope table. To increase the sensitivity even further it has been taken into account that the microscope light source heats up the emulsion slightly. To establish a stable situation, the emulsion plate was exposed to the light source an hour before the actual measurement.

After corrections for global shrinkage and local distortion of the emulsion, the grain-by-grain measurement provides a three dimensional view of the vertex, the tracks and the decay angles. The decay angles are found to be (39.5 ± 2.4) mrad for the first and (87.3 ± 1.2) mrad for the second kink. The distance from the primary vertex to the first decay is $68 \mu\text{m}$ and from the first to the second kink $147 \mu\text{m}$. The first decay is located close to the surface of an emulsion plate ($\sim 16 \mu\text{m}$ distance).

In view of the short flight lengths with the measured momenta and decay angles, we postulate that it represents the neutrino induced production of a charmed particle (D or D_s meson) at the primary vertex.

Following the background studies from the previous paragraph the decay chain $D_s \rightarrow \tau \rightarrow \mu$ hypothesis is clearly favoured compared with other decays that could produce a double kink. Furthermore, the measured decay angles and momenta of the candidate event are consistent with this hypothesis.

Taking all observations together, the most probable explanation is that the observed double kink signature originates from the decays $D_s^+ \rightarrow \tau^+ \nu_\tau$, $\tau^+ \rightarrow \mu^+ \nu_\mu \bar{\nu}_\tau$.

Then, given that the decay of a D_s^+ is at the origin of the double kink event, it is plausible that the energy measured in the electromagnetic part of the calorimeter can be associated with the conversion of a photon seen as the secondary interaction vertex in the target region. These two observations lead to the hypothesis of a D_s^{*+} production with a radiative decay $D_s^{*+} \rightarrow D_s^+ \gamma$.

Kinematical reconstruction

In addition to the μ^- and the D_s^{*+} observed at the primary vertex, we assume that a recoil neutron escapes from the target nucleus and interacts in the calorimeter, leaving a visible energy of (0.53 ± 0.22) GeV. This energy deposition, the topology of the event and the kinematics constrain the neutron momentum to $0.7 \text{ GeV} \leq p_n \leq 1.8 \text{ GeV}$.

Conservation of transverse momentum at the primary vertex then allows

With a lower limit of the transverse τ momentum p_τ^T one obtains an upper limit for the ν_τ mass:

$$m_\nu^2 < m_{D_s}^2 + m_\tau^2 - 2m_{D_s} \sqrt{p_\tau^{T2} + m_\tau^2}. \quad (5.7)$$

Unfortunately, with the topology of our observed event, the derived limit on the ν_τ mass can be set at 90% CL only at the kinematical limit of $m_{\nu_\tau} \leq 191$ MeV compared with the presently best measured limit [5] of $m_{\nu_\tau} \leq 18.2$ MeV at 95% CL.

5.6 Cross section

The diffractive D_s^* production can be derived by evaluating

$$\frac{\sigma_{D_s^*}^{diff}}{\sigma_{CC}} = \frac{N_{obs}}{N_{CC} B_{D_s \rightarrow \tau \nu_\tau} B_{\tau \rightarrow \mu \nu_\mu \nu_\tau}} \times \frac{1}{A^{Rec} A^{Frac} A^{AS} A^{MS}}. \quad (5.8)$$

With the quantities

$N_{CC} = 544683$	corresponding number of CC events
$B_{D_s \rightarrow \tau \nu_\tau} = 0.07 \pm 0.04$	branching ratio $D_s \rightarrow \tau$ [29]
$B_{\tau \rightarrow \mu \nu_\mu \nu_\tau} = 0.174 \pm 0.001$	branching ratio $\tau \rightarrow \mu$ [29]
$A^{Rec} \simeq 0.65 \pm 0.07$	finding efficiency in the electronic detector
$A^{Frac} \simeq 0.55$	fraction of emulsion analyzed
$A^{AS} \simeq 0.60 \pm 0.02$	location efficiency in emulsion
$A^{MS} \simeq 0.96 \pm 0.03$	manual scanning efficiency

(5.9)

Associating with the observed event a poisson error and with the branching ratios and correction factors a gaussian error, we can calculate with our single event an upper limit for the diffractive D_s^* production

$$\frac{\sigma_{D_s^*}^{diff}}{\sigma_{CC}} \leq 4.6 \times 10^{-3} \text{ at } 90\% \text{ CL}. \quad (5.10)$$

Comparison with results of other experiments

All data from the bubble chamber experiments WA21, WA25, WA59 and E180 were combined in a search for diffractive D_s^* and D_s meson production [41],

which could not be unambiguously distinguished. Six candidates lead to a diffractive production ratio (for D_s and D_s^* together) of

$$\frac{\sigma_{D_s D_s^*}^{diff}}{\sigma_{CC}} B_{D_s \rightarrow \Phi \pi} = (1.03 \pm 0.27) \times 10^{-4}. \quad (5.11)$$

With $B_{D_s \rightarrow \Phi \pi} = (3.6 \pm 0.9) \times 10^{-2}$ [29], the cross section ratio becomes

$$\frac{\sigma_{D_s D_s^*}^{diff}}{\sigma_{CC}} = (2.86 \pm 1.46) \times 10^{-3}. \quad (5.12)$$

Recently, the NuTeV collaboration published evidence for diffractive charm production [42], they also could not distinguish D_s^* from D_s . The calculated cross section is

$$\frac{\sigma_{D_s + D_s^*}^{diff}}{\sigma_{CC}} = (3.2 \pm 0.6) \times 10^{-3}. \quad (5.13)$$

The 90% CL upper limit (Equation 5.10) on the basis of our single event is in agreement with the other measurements. For the upcoming CHORUS Phase II scanning data, more diffractive events are expected. Then we will be able to measure the cross section ratio - rather than to put an upper limit - and to make a comparison with the other measurements.

Although not the main goal of the CHORUS experiment, this type of measurement is of interest. It could make use of well-developed techniques - the reconstruction and identification developed for the neutrino production search. CHORUS and E811 at Fermilab (USA) are the only experiments where charged particles are heretically identified in the analysis, both at the production and at the decay stage.

Two different production mechanisms of charmed particles by interactions are analyzed: deep-inelastic and diffractive charm production.

To separate any background, the deep-inelastic charm production study concentrates on the neutral decay channels of the charmed hadrons. This results in a data sample of 143 observed charm decays. With this sample the fractional charm production (with neutral decay) per charged-current interaction is measured to be $(4.8 \pm 3.6 \pm 5.7) \times 10^{-3}$. This charm production as a function of the neutrino energy is in agreement with other experiments. The cross section ratio of neutral and charged charmed hadrons as a function of the neutrino energy shows at low energies a tendency of enhanced production of charged with respect to the neutral charmed hadrons.

Discussing the charm production cross-sections with the above results, model

the χ^2 value. The χ^2 value is calculated as follows:

$$\chi^2 = \sum_{i=1}^N \frac{(N_i - \mu_i)^2}{\mu_i} \quad (5.11)$$

where N_i is the number of events in the i th bin, μ_i is the expected number of events in the i th bin, and N is the total number of bins. The χ^2 value is then compared to the χ^2 distribution to determine the probability of the fit being a good fit.

The χ^2 value is then used to determine the probability of the fit being a good fit. The χ^2 value is then compared to the χ^2 distribution to determine the probability of the fit being a good fit.

The χ^2 value is then used to determine the probability of the fit being a good fit. The χ^2 value is then compared to the χ^2 distribution to determine the probability of the fit being a good fit.

$$\chi^2 = \sum_{i=1}^N \frac{(N_i - \mu_i)^2}{\mu_i} \quad (5.12)$$

The χ^2 value is then used to determine the probability of the fit being a good fit. The χ^2 value is then compared to the χ^2 distribution to determine the probability of the fit being a good fit.

The χ^2 value is then used to determine the probability of the fit being a good fit. The χ^2 value is then compared to the χ^2 distribution to determine the probability of the fit being a good fit.

$\mu_{D_s^*} = 0.07 \pm 0.04$	branching ratio $D_s^* \rightarrow \mu \gamma$
$\mu_{D_s} = 0.17 \pm 0.08$	branching ratio $D_s \rightarrow \mu \gamma$
$A^{D_s^*} = 0.65 \pm 0.07$	branching ratio in the electron channel
$A^{D_s} = 0.55$	branching ratio in the electron channel
$A^{D_s^*} = 0.00 \pm 0.02$	branching ratio in the muon channel
$A^{D_s} = 0.00 \pm 0.02$	branching ratio in the muon channel

Comparing with the observed event a point error and with the branching ratio at 1 σ level, we can calculate the upper limit for the D_s^* production

$$\frac{\mu_{D_s^*}}{\mu_{D_s}} \leq 1.6 \times 10^{-2} \text{ at } 90\% \text{ CL} \quad (5.13)$$

Comparison with results of other experiments

There have been several experiments WA21, WA25, WA39 and E187 which have measured the branching ratio for D_s^* and D_s meson production [1].

Summary

The neutrino is one of the known fundamental particles. It is only very weakly interacting with matter, hence it is difficult to detect. Since decades, in experiments all around the world, neutrinos are used as a probe and they are subject of research to reveal their properties.

The CHORUS experiment at CERN has been designed to search for neutrino oscillation of the type $\nu_\mu \rightarrow \nu_\tau$. It uses 720 kg of nuclear emulsion simultaneously as a target and as a tracker in three dimensions with sub- μm resolution. The emulsion information is combined with electronic detector information, e.g. energy and momentum measurements.

In this thesis charm production by neutrinos is studied. Although not directly concerned with the main purpose of the CHORUS experiment, this work could be included in the CHORUS programme. It could make use of—and possibly contribute to—the measurements and techniques developed for the neutrino oscillation search. CHORUS and E531 at Fermilab (USA) are the only experiments where charmed particles can be directly observed in the emulsion, both at the production and at the decay vertex.

Two different production mechanisms of charmed particles by neutrinos are analyzed: deep-inelastic and diffractive charm production.

To suppress any background, the deep-inelastic charm production study concentrates on the muonic decay channels of the charmed hadrons. This results in a data sample of 132 observed charm decays. With this sample the fractional charm production (with muonic decay) per charged-current interaction is measured to be $(4.6 \pm 0.4 \pm 0.7) \times 10^{-3}$. This charm production as a function of the neutrino energy is in agreement with other experiments. The cross section ratio of neutral and charged charmed hadrons as a function of the neutrino energy shows at low energies a tendency of enhanced production of charged with respect to the neutral charmed hadrons.

Describing the charm production cross section with the slow rescaling model,

results in a charm quark mass of $m_c = (1.6 \pm 0.8)$ GeV. Parameterizing the charm hadronization with the Peterson fragmentation model gives for the fragmentation parameter $\epsilon_P = 0.12 \pm 0.02 \pm 0.06$. The integrated strangeness-down ratio in the nucleon is measured to be $s/d = 0.024 \pm 0.011 \pm 0.008$. Combining information of charged charm production from E531 with our observed neutral over charged charm ratio leads to a weak mixing angle value $V_{cd} = 0.247 \pm 0.028$.

The diffractive production search focuses on D_s^* mesons with subsequent decays $D_s^* \rightarrow D_s \rightarrow \tau \rightarrow \mu$. In this thesis we present the first observation of a neutrino induced charged-current charm production event showing this unique decay signature. A complete analysis of this single event is possible thanks to the exceptional tracking capabilities of the CHORUS hybrid emulsion detector. At the primary vertex no nuclear break-up is observed. The structure of the whole event, the measured $Q^2 = (0.8 \pm 0.1)$ GeV² and $|t| = (1.1 \pm 0.4)$ GeV² point to diffractive D_s^* production on a nucleon. The observation of one event is expressed in an upper limit of the cross section per charged-current interaction of 4.6×10^{-3} at 90% CL.

Our results show that the CHORUS data can contribute significantly to the knowledge of charm production by neutrinos. They motivate a dedicated charm study, including the hadronic decay channels. This can lead to a ten times bigger charm sample using the emulsion data from the Phase II CHORUS emulsion scanning and analysis. For the first time, it then may also become possible to study simultaneously deep-inelastic and diffractive charm production by neutrinos in detail.

Samenvatting

Het neutrino is een van de bekende fundamentele deeltjes. Het ondergaat alleen zwakke wisselwerking met materie, daarom is het moeilijk waar te nemen. Sedert tientallen jaren worden in experimenten over de hele wereld neutrino's gebruikt voor onderzoeken en ze worden zelf onderzocht op hun eigenschappen.

Het CHORUS experiment in CERN is ontworpen voor het zoeken naar neutrino oscillaties van het type $\nu_\mu \rightarrow \nu_\tau$. Het gebruikt 720 kg kern-emulsie zowel als trefplaat als voor het meten van deeltjessporen in drie dimensies met sub- μm oplossend vermogen. De emulsiegegevens worden gecombineerd met de informatie afkomstig van de elektronische detectoren, bijvoorbeeld de energie- en impulsmeting.

Dit proefschrift beschrijft een studie van charmproductie door neutrino's. Hoewel niet direct samenhangend met het hoofddoel van het CHORUS experiment, kon dit werk worden opgenomen in het CHORUS programma. Het kon gebruik maken—en mogelijk bijdragen aan—de metingen en technieken ontwikkeld ten behoeve van het zoeken naar neutrino oscillaties. CHORUS en E531 in het Fermilab (VS) zijn de enige experimenten waarbij gecharmeerde deeltjes direct in emulsie kunnen worden waargenomen zowel bij de productie vertex als bij het hadronische verval.

Twee verschillende productiemechanismen van gecharmeerde deeltjes door neutrino's worden geanalyseerd: diep-inelastische en diffractieve productie.

Om alle achtergrond te onderdrukken concentreert de studie van diep-inelastische charmproductie zich op de kanalen met muonisch verval van gecharmeerde hadronen. Dit resulteert in een verzameling meetgegevens voor 132 waargenomen gevallen van charm verval. Met deze verzameling wordt de fractionele charmproductie (met muonisch verval) per geladen-stroom interactie gemeten als $(4.6 \pm 0.4 \pm 0.7) \times 10^{-3}$. De charmproductie als functie van de neutrino energie is in overeenstemming met andere experimenten. De verhouding van reactiedoorsneden voor neutrale en geladen gecharmeerde hadronen als

functie van de neutrino-energie vertoont bij lage energie de tendens van een toegenomen productie van geladen t.o.v. neutrale gecharmeerde hadronen.

Het beschrijven van de reactiedoorsnede voor charmproductie met het 'slow rescaling' model, resulteert in een charm-quark-massa van $m_c = (1.6 \pm 0.8)$ GeV. Parametrisering van de charmhadroneisatie met het fragmentatiemodel van Peterson geeft voor de fragmentatieparameter $\epsilon_P = 0.12 \pm 0.02 \pm 0.06$. De geïntegreerde strangeness-down verhouding in het nucleon wordt gemeten als $s/d = 0.024 \pm 0.011 \pm 0.008$. Het combineren van gegevens van E531 betreffende geladen charmproductie met onze gevonden verhouding voor neutrale en geladen charmproductie leidt tot een waarde voor de menghoek van de zwakke wisselwerking $V_{cd} = 0.247 \pm 0.028$.

Het zoeken naar diffractieve productie richt zich op D_s^* mesonen met verval $D_s^* \rightarrow D_s \rightarrow \tau \rightarrow \mu$. In dit proefschrift geven we voor het eerst een waargenomen gebeurtenis weer van charmproductie in een geladen-stroom interactie van een neutrino, waarbij deze unieke vervals-signatuur zichtbaar is. Een volledige analyse van deze enkele gebeurtenis is mogelijk dankzij de uitzonderlijke mogelijkheden van de CHORUS hybride emulsiedetector om deeltjessporen te bepalen. Bij de primaire vertex wordt geen kern-breakup waargenomen. De structuur van het geheel aan waarnemingen bij de gebeurtenis, de gemeten $Q^2 = (0.8 \pm 0.1)$ GeV² en $|t| = (1.1 \pm 0.4)$ GeV² wijzen op diffractieve productie aan een nucleon. De waarneming van een enkele gebeurtenis wordt uitgedrukt in een bovengrens voor de reactiedoorsnede per geladen-stroom interactie van 4.6×10^{-3} bij 90% CL.

Onze resultaten tonen aan dat de CHORUS meetgegevens significant kunnen bijdragen aan de kennis van charmproductie door neutrino's. Zij motiveren een op charm toegesneden studie, inclusief de kanalen van hadronisch verval. Dit kan leiden tot een tienmaal grotere verzameling charm gegevens gebruikmakend van de Phase II CHORUS emulsie-scanning en analyse. Voor het eerst wordt het dan ook mogelijk tegelijk diep-inelastische en diffractieve charmproductie door neutrino's in detail te bestuderen.

Bibliography

- [1] F. Wilczek et B. Devine. Quoted in 'Longing for Harmonies'. (New York, Norton), 64, (1988).
- [2] C. Sutton. Spaceship neutrino. Cambridge University Press, (1992).
- [3] O. Adriani et al. *Phys. Lett.* **B292**, 463 (1992).
- [4] M. Nakamura et al. *Nucl. Phys. Proc. Suppl.* **77**, 259 (1999).
- [5] D.E. Groom et al. *Eur. Phys. J.* **C15** (2000).
- [6] Y. Fukuda et al. *Phys. Rev. Lett.* **81**, 1562 (1998).
- [7] J. Ellis. hep-ph/0008334, (2000).
- [8] E. Eskut et al. CERN-EP/2000-147, (2000).
- [9] J.G. Learned, S. Pakvasa, et T.J. Weiler. *Phys. Lett.* **B207**, 79 (1988).
- [10] J.M. Conrad, M.H. Shaevitz, et T. Bolton. *Rev. Mod. Phys.* **70**, 1341 (1998).
- [11] H. Georgi et H.D. Politzer. *Phys. Rev.* **D14**, 1829 (1976).
- [12] O. Nachtmann. *Nucl. Phys.* **B78**, 455 (1974).
- [13] B. Andersson, G. Gustafson, et B. Söderberg. *Z. Phys.* **C20**, 317 (1983).
- [14] P.D.B. Collins et T.P. Spiller. *Nucl. Phys.* **11**, 1289 (1985).
- [15] C. Peterson et al. *Phys. Rev.* **D27**, 105 (1983).
- [16] M. Aguilar-Benitez et al. *Phys. Lett.* **B123**, 99 (1983).
- [17] T. Bolton. Preprint KSU-HEP/97-04, hep-ex/9708014, (1997).
- [18] S.J. Brodsky et al. *Phys. Rev.* **D50**, 3134 (1994).

- [19] M. Strikman. private communication. (2000).
- [20] A. Mueller. private communication. (2000).
- [21] M.K. Gaillard, S.A. Jackson, et D.V. Nanopoulos. *Nucl. Phys.* **B102**, 326 (1976).
- [22] C.A. Piketty et L. Stodolsky. *Nucl. Phys.* **B15**, 571 (1970).
- [23] M.S. Chen, F.S. Henyey, et G.L. Kane. *Nucl. Phys.* **B118**, 345 (1977).
- [24] A. Bartl, H. Fraas, et W. Majerotto. *Phys. Rev.* **D16**, 2124 (1977).
- [25] M.K. Gaillard et C.A. Piketty. *Phys. Lett.* **B68**, 267 (1977).
- [26] B.Z. Kopeliovich et P. Marage. *J. Mod. Phys.* **A8**, 1513 (1993).
- [27] O. Melzer. CERN-THESIS/98-012, (1998).
- [28] L.M. Sehgal et D. Rein. private communication. (1997).
- [29] C. Caso et al. *Eur. Phys. J.* **C3** (1998).
- [30] Z. Bai et al. *Phys. Rev. Lett.* **65**, 686 (1990).
- [31] E. Vella et al. *Phys. Rev. Lett.* **48**, 1515 (1982).
- [32] T. Sjöstrand. *Comp. Phys. Commun.* **82**, 74 (1994).
- [33] M. Bargiotti et al. hep-ph/0001293, (2000).
- [34] N. Ushida et al. *Nucl. Instr. and Meth.* **224**, 50 (1984).
- [35] W.K. Sakumoto et al. *Nucl. Instr. and Meth.* **A294**, 179 (1990).
- [36] B.J. King et al. *Nucl. Instr. and Meth.* **A302**, 254 (1991).
- [37] A.N. Diddens et al. *Nucl. Instr. and Meth.* **178**, 27 (1980).
- [38] M. Holder et al. *Nucl. Instr. and Meth.* **148**, 235 (1978).
- [39] K. De Winter et al. *Nucl. Instr. and Meth.* **A278**, 670 (1989).
- [40] J. Altegoer et al. *Nucl. Instr. and Meth.* **A404**, 96 (1998).
- [41] P. Marage et al. *Z. Phys.* **C58**, 55 (1993).
- [42] T. Adams et al. FERMILAB-Pub/99-269, (1999).

- [43] M. Kaku. Quoted in 'hyperspace'. Oxford University press, 30, (1995).
- [44] R.G.C. Oldeman. Ph.D. Thesis, NIKHEF, (2000).
- [45] E. Eskut et al. *Nucl. Instr. and Meth.* **A401**, 7 (1997).
- [46] E. Heijne. Cern yellow report. 83-06, (1983).
- [47] G. Acquistapace et al. CERN-ECP/95-14, (1995).
- [48] S. Sorrentino. CHORUS internal report 980005, (1998).
- [49] B. Van de Vyver et P. Zucchelli. *Nucl. Instr. and Meth.* **A385**, 91 (1997).
- [50] M.C. Gonzalez-Garcia et J.J. Gomez-Cadenas. *Phys. Rev.* **D55**, 1297 (1997).
- [51] S. Aoki et al. *Nucl. Instr. and Meth.* **A447**, 361 (2000).
- [52] P. Annis et al. CERN-EP/97-100, (1997).
- [53] P. Annis et al. *Nucl. Instr. and Meth.* **A386**, 72 (1997).
- [54] F. Bergsma et al. *Nucl. Instr. and Meth.* **A357**, 243 (1994).
- [55] J. Dupraz, D. Saltzberg, et G.V. Beek. CERN-PPE/96-179, (1996).
- [56] D. Acosta et al. *Nucl. Instr. and Meth.* **A308**, 481 (1991).
- [57] S. Buontempo et al. *Nucl. Instr. and Meth.* **A349**, 70 (1994).
- [58] E. di Capua et al. *Nucl. Instr. and Meth.* **A378**, 221 (1996).
- [59] M.G.v. Beuzekom et al. CERN-EP/98-131, (1998).
- [60] W.H. Barkas. Nuclear research emulsion. Academic Press New York and London, (1963).
- [61] S. Aoki et al. *Nucl. Instr. and Meth.* **B51**, 466 (1990).
- [62] O. Melzer et al. *IoP Proc. EPS HEP99 - Tampere*, 1022 (1999).
- [63] www.thomson-csf.com.
- [64] www.jenoptik.com.
- [65] www.lsi-dsp.com.
- [66] www.micos-online.com.

- [67] J. Brunner. Chorus offline manual. (1998).
- [68] G. Zacek et H. Øveras. Charm II offline manual, (1989).
- [69] H. Eichinger et M. Regler. Yellow Report CERN, (1981).
- [70] G. Heyboer. CHORUS internal report 960006, (1996).
- [71] L.S. Brown et D.L. Nordstrom. *Phys. Rev.* **D50**, 1251 (1994).
- [72] H. Harari. *Proc. 13th Int.Conf. on Neutrino Physics and Astrophysics, Boston*, 574 (1988).
- [73] P. Zucchelli. Ph.D. Thesis, Univerit degli Studi di Ferrara, Italy, (1992).
- [74] G. Ingelman, A. Edin, et J. Rathsman. hep-ph/9605286, (1996).
- [75] M. Glueck, E. Reya, et A. Vogt. *Z. Phys* **C67**, 433 (1995).
- [76] CERN. GEANT - CERN Program Library Long Writeup.
- [77] A. Artomonov et P. Gorbunov. CHORUS internal note 97029.
- [78] G. Brooijmans. Ph.D. Thesis, Universit catholique de Louvain, (1998).
- [79] H. Abramowicz et al. *Z. Phys.* **C15**, 19 (1982).
- [80] S.A. Rabinowitz. *Phys. Rev. Lett.* **70**, 134 (1993).
- [81] P. Astier et al. CERN-EP/2000-72, (2000).
- [82] K.v.d. Poel. Ph.D. Thesis, NIKHEF, (1999).
- [83] A. Höcker et V. Kartvelishvili. *Nucl. Instr. and Meth.* **A372**, 469 (1996).
- [84] P. Vilain et al. *Eur. Phys. J.* **C11**, 19 (1999).
- [85] N. Ushida et al. *Phys. Lett.* **B206**, 380 (1988).
- [86] M. Jonker et al. *Phys. Lett.* **B107**, 241 (1981).
- [87] S.G. Frederiksen. Ph.D. Thesis, University of Ottawa, (1987).
- [88] B.J. Edwards et T.D. Gottschalk. *Nucl. Phys.* **B186**, 309 (1981).
- [89] G. Altarelli, R.K. Ellis, et G. Martinelli. *Nucl. Phys.* **B157**, 461 (1979).
- [90] C. Foudas et al. *Phys. Rev. Lett.* **64**, 1207 (1990).

- [91] A.O. Bazarko et al. *Z. Phys.* **C65**, 189 (1995).
- [92] K. Kodama et al. *Nucl. Instr. and Meth.* **B93**, 340 (1994).
- [93] A. Bülte et al. Charon experiment - www.cern.ch/charon. (2000).

Acknowledgements

I would like to thank the following for their support: Dr. Jim Gaudin, for my "sponsor", Dr. Sigmund, for having given me the chance to write this book. They provided me with the best possible conditions and opportunities during my time at CERN and elsewhere. I would also like to thank the CERN-BUS collaboration for the exceptional organized experiment that I part of which I worked with it. I would especially like to thank the following colleagues:

- E. Nagy, for his hospitality and support during my several stays in Nagoya.
- A. Turchetti, who taught me the first steps of scientific analysis and got me interested in diffractive production;
- K. Wroble, for his optimism and experienced advice;
- J. Farnaud, for always being available as the CERN group leader to help with the logistical problems that I encountered during my stay at CERN;
- P. Skvira, for his advice and support;
- A. Bülte, for all the discussions about physics and the normal part, and the great times spent with Kira and Mia. Thanks to Sergey Ivanov that M. de Jong and H. Wickens, with whom I shared many interesting discussions and coffee, and who gave me insight into the workings of the heterozygous charon software;
- D. Salsberg, for his physics ideas, sense of humor, showing the collaboration the "American working approach", and for giving me all the needed information about the RAINIX;
- I. Litvack and M. Lohmann, for helping me set up the DAQ and help with the TORUS test beam, help from Yury Lamber and the jet team in my home, S. Bortolotto;

- [57] J. Gruber, *Chosen official journal*, (1969).
- [58] G. Huet et al. *Orsay Report*, (1969).
- [59] H. Bichard et al. *Orsay Report*, (1969).
- [60] G. Huet et al. *CHORUS internal report*, (1969).
- [61] L.S. Brown et al. *Orsay Report*, (1969).
- [62] M. Hara, *Proc. 19th Int. Conf. on Nuclear Physics and Elementary Particles*, 374 (1969).
- [63] P. Zuchelli, Ph.D. Thesis, Universit degli Studi di Padova, Italy, (1969).
- [64] G. Israelian, A. Lodi et al. *Radiation Rep-69/696396*, (1969).
- [65] M. Goulet, E. Nays, et al. *Veget. J. Pays-Cor*, 333 (1969).
- [66] CERN, GRANT - CERN Program Library Long Writing.
- [67] A. Antonov et al. *CHORUS internal note*, (1969).
- [68] G. Brochmann, Ph.D. Thesis, Université catholique de Louvain, (1969).
- [69] H. Abramowicz et al. *Z. Phys. C10*, 19 (1969).
- [70] S.A. Katsenelenbaum, *Phys. Rev. Lett.* 70, 134 (1969).
- [71] P. Adami et al. *CERN-EP/1969.71*, (1969).
- [72] K. von Paul, Ph.D. Thesis, KERNZ, (1969).
- [73] A. Hübner et al. *Nucl. Instr. and Meth.* 2372, 469 (1969).
- [74] F. Nijssen et al. *Rev. Phys. J.* C11, 19 (1969).
- [75] A. Lodi et al. *Phys. Lett.* B266, 380 (1969).
- [76] M. Tschudi et al. *Phys. Lett.* B107, 367 (1969).
- [77] F. G. Koenig, Ph.D. Thesis, University of Ottawa, (1969).
- [78] R. S. Thayer et al. *Orsay Report*, (1969).
- [79] G. Huet et al. *Phys. Lett.* B107, 367 (1969).
- [80] G. Huet et al. *Phys. Lett.* B107, 367 (1969).
- [81] G. Huet et al. *Phys. Rev. Lett.* 64, 1207 (1969).

Acknowledgements

I would like to take this opportunity to thank my supervisor, R. van Dantzig, and my 'promotor', J. Engelen, for having given me the chance to write this thesis. They provided me with the best possible conditions and opportunities during my time at CERN and NIKHEF. I would also like to thank the CHORUS collaboration for the enjoyment and great experiences that I gained while involved with it. I would especially like to thank the following colleagues:

K. Niwa, for his hospitality and support during my several stays in Nagoya;

P. Zuchelli, who taught me the first steps of scientific analysis and got me interested in diffractive production;

K. Winter, for his assistance and experienced advice;

J. Panman, for always being available as the CERN group leader to help with the logistical problems that I encountered during my stay at CERN;

P. Strolin, for his advice and support;

A. Bülte, for all the discussions about physics and the normal world, and the great times spent with him and Mrs. Newton in Sergy-Haut castle;

M. de Jong and R. Oldeman, with whom I shared many inspiring discussions and coffees, and who gave me insight into the workings of the honeycomb chamber software;

D. Saltzberg, for his physics ideas, sense of humour, showing the collaboration the 'American working approach', and for giving me all the inside information about the RASNIK;

J. Uiterwijk and M. Litmaath, for helping to set up the DAQ and hardware in the TOSCA test beam's baby-honeycomb chamber, and the test beam project leader, S. Ricciardi;

J.P. Fabre and E. Tsesmelis, for their help and support during the CERN open day project's preparation and completion;

Y. Narita, T. Toshito, Y. Obayashi, M. Komatsu, T. Kozaki, T. Nakano and especially O. Sato, who were always helpful answering my questions concerning emulsion and scanning (and translating the Japanese error messages when Windows NT crashed);

Y. Kotaka, for the days (and nights) in the emulsion lab spent trying to apply chemical treatments to emulsion plates;

K. Kodama for making the 'special high precision microscope stage' work again;

Y. Narita, A. Bülte, J. Herin, Y. Naruse, M. Vander Donckt, O. Sato and T. Toshito, for contributing to the manual charm scanning;

D. Frekers, whose lecture created my interest in experimental neutrino physics, for his support and backing during my application to CERN;

B. van de Vyver, J. Uiterwijk, I. M. Papadopoulos, M. Doucet, B. Friend and E. Pesen, for the dynamic working atmosphere in the microscope project;

H. Meinhard, D. Cussans and J. Brunner, for helping with hardware and software problems;

B. Saitta, C. Weinheimer and G. Brooijmans, for always having good ideas for solving physics problems;

M. Strikman, A. Mueller, D. Rein and L. Sehgal, for the discussions on the theoretical description of diffractive production.

V. Mexner, S. Muis, M. Mulders, S. Peeters, C. Simani and J. Visser, for the nice chats at coffee time;

J. Konijn and J. Visschers, for their support and help;

S. Anthony and H. Gruber, for always being helpful in solving various problems that I encountered during my stay at CERN, ranging from administrative matters to correcting my English writing;

Last, but not least, I would like to thank my family for their continuous support and Isabell for her understanding during my restless years of study.

